SUBSURFACE EXPRESSION OF A TERTIARY SALT WELD, GULF OF MEXICO

Christopher A-L. Jackson[1*]
Yue Zhang[1]
Donald A. Herron[2]
Peter J.R. Fitch[1]

[1]*Basins Research Group (BRG), Department of Earth Science and Engineering, Imperial College London, UK*

[2]*Consultant, Sugar Land, Texas, USA*

**Corresponding author email: c.jackson@imperial.ac.uk*

ABSTRACT

Salt welds form due to salt expulsion and thinning by mechanical (e.g. salt flow) and/or chemical (e.g. salt dissolution) processes. Despite being ubiquitous in salt-bearing sedimentary basins, where they may trap large volumes of hydrocarbons, little is published on weld thickness and composition. We here use 3D seismic reflection, borehole, and biostratigraphic data from the Atwater Valley protraction area of the northern Gulf of Mexico to constrain the thickness and composition of a tertiary salt weld. Seismic data image an 'apparent weld' (sensu Wagner and Jackson, 2011) at the base of a Plio-Pleistocene minibasin that subsided into allochthonous salt. Borehole data indicate the weld is actually 'incomplete', being c. 24 m thick, and containing an upper 5 m thick halite and a lower 15 m thick halite, separated by a 4 m thick mudstone. The age and origin of the intra-weld mudstone is unclear, although we speculate it is either: (i) Late Jurassic, representing material transported upwards from the autochthonous level within a feeder, and subsequently trapped as allochthonous salt thinned and welded, or, perhaps more likely; (ii) Pliocene, representing a piece of salt carapace reworked from the top of and eventually trapped in, the now locally welded sheet. We show 3D seismic reflection data may not resolve salt weld thickness, with the presence of relatively thin remnant salt lending support to models of welding based on viscous flow. Furthermore, the halite-dominated character of the weld supports the hypothesis that tectonic purification may occur during salt flow.

INTRODUCTION

Salt welds are ubiquitous in salt-bearing sedimentary basins, forming due to expulsion of salt from

below or between minibasins (Jackson and Cramez, 1989). Based on their structural position and attitude, welds are described as 'primary' (i.e. subhorizontal, joining strata originally above and below autochthonous salt), 'secondary' (i.e. subvertical, joining minibasins originally situated either side of squeezed and now-evacuated salt diapirs, or 'tertiary' (i.e. subhorizontal, joining strata originally above and below allochthonous salt (Jackson and Cramez, 1989). Depending on how much salt they contain (or are inferred to contain), welds are also described as 'complete' (i.e. contains no remnant salt; cf. Jackson and Cramez, 1989), 'incomplete' (i.e. contains up to 50 m of remnant salt), 'discontinuous' (i.e. contains complete and incomplete parts), or 'apparent' (i.e. appears free of salt at a particular scale of observation (Wagner, 2010; Hudec and Jackson, 2011; Wagner and Jackson, 2011; Rowan et al., 2012; Jackson et al., 2014).

Salt welds are economically important because, depending on their thickness and composition, they may represent barriers to fluid flow, and thus trap hydrocarbon accumulations (Rowan, 2004). Furthermore, weld thickness and composition reveal much about salt rheology and patterns of internal deformation (see below; see also Kupfer, 1968; Wagner and Jackson, 2011; Jackson et al., 2014). Despite their importance and ubiquity, we have a rather poor understanding of the thickness or composition of subsurface welds; in some basins, this reflects a lack of borehole penetrations or, in relatively densely drilled basins, such as the Gulf of Mexico, restricted access to these data. Where these data are available, such as in the Santos Basin, offshore Brazil they indicate that even high-quality 3D seismic reflection data may be unable to resolve the thickness or composition of welds. These data also show that primary welds may lack true 'salt' (e.g. halite and potash), and instead contain carbonate, anhydrite, and sandstone (Jackson et al., 2014; see also fig. 17 in Wagner and Jackson, 2011). This lithological partitioning suggests preferential expulsion of the more mobile halite and potash salt from the autochthonous layer into flanking diapirs during viscous flow and welding, and/or preferential dissolution of these components, which, in addition to being the most mobile, are also the most soluble. This process, which is termed 'differential purification by movement' by Kupfer (1968), implies that successive periods of salt flow, for example as salt ascends from autochthonous to allochthonous levels, will lead to relative enrichment in the more mobile components (e.g. halite, potash salts) of the original salt layer. This observation supports analytical and numerical models based on viscous-thinning of the salt during welding (Wagner and Jackson, 2011), which conclude it is difficult to fully remove salt from a weld by viscous flow alone because of boundary drag along the salt contacts (see also Cohen and Hardy, 1996; Hudec and Jackson, 2007). More specifically, the models of Wagner and Jackson (2011) suggest that a weld may contain anywhere from <1 m to up to c. 50 m of remnant salt, although they recognize that model-based predictions of remnant evaporite thickness in salt welds has hitherto been difficult to test due to a lack of data from natural welds (see Wagner, 2010; Hoetz et al., 2011; Liro and Holdaway, 2011; Rowan et al., 2012).

We here use 3D seismic reflection, borehole and biostratigraphic data from Block 8 in the Atwater Valley protraction area of the Gulf of Mexico (Fig. 1) to characterise the subsurface expression of a tertiary salt weld. 3D seismic reflection data allow us to define the geophysical expression and structural context of the weld, whereas borehole data allow us to constrain weld thickness and composition. Biostratigraphic data allow us to establish the age of weld-flanking strata, and to place the development of the weld in the regional salt-tectonic framework. More specifically, our data allow us to test the following two hypotheses: (i) that allochthonous salt, and laterally equivalent tertiary welds, should be relatively enriched in the more mobile lithologies typically encountered at autochthonous levels; and (ii) that only several tens of metres of remnant salt should remain in a seismically defined weld. We then discuss the implications of our results for petroleum systems development in sedimentary basins.

GEOLOGICAL SETTING

The Gulf of Mexico formed in response to Triassic-Early Cretaceous rifting (e.g., Pindell and Dewey, 1982; Kneller and Johnson, 2011; Hudec et al., 2013b). Extension and subsidence allowed establishment of a restricted marine seaway, within which the Louann salt (Middle Jurassic) was deposited (e.g., Hazzard et al., 1947; Humphris, 1978; Salvador, 1987; Kneller and Johnson, 2011; Hudec et al., 2013a). Since then, in the northern Gulf of Mexico, this salt layer flowed to form a complex array of salt diapirs and sheets, canopies and welds, largely in response to loading of the autochthonous and then allochthonous salt levels by Mesozoic to Cenozoic sediments, now preserved in predominantly clastic-filled minibasins (Fig. 1B) (e.g., Diegel et al., 1995; Peel et al., 1995; Rowan, 1995; Pilcher et al., 2011).

Our study area is located in Block 8 of the Atwater Valley protraction area, on the south-western flank of the Mississippi Fan, northern Gulf of Mexico (Fig. 1). Water depths range from 650 to 1150 m. Here, the salt-tectonic framework is dominated by: (i) Miocene and older rocks contained in primary minibasins that overlie autochthonous salt; (ii) a series of diapiric feeders that separate primary minibasins, and that connect upward to feed salt sheets within a regionally extensive canopy extending southwards to the Sigsbee Escarpment; and (iii) Plio-Pleistocene rocks contained in secondary minibasins that subsided into allochthonous salt and that locally welded to underlying primary minibasins (Fig. 1B).

DATASET

Seismic Data

The seismic volume used in this study is a subset of a large regional 3D survey, composed of multiple

narrow-azimuth 3D seismic data sets acquired in 1995-1998 and subsequently reprocessed as a single survey in 2008. This subset covers an area of approximately 550 km^2 in the southwestern Mississippi Canyon (MC) and northwestern Atwater Valley (AT) protraction areas in the east-central Gulf of Mexico (Fig. 1A). 3D Kirchhoff prestack depth migrated (KPSDM) data migrated using an isotropic velocity model, with a sample rate of 10 m, record length of 15 km, and final bin size of 25m x 25 m, were used for interpretation. The data were processed to zero phase, and all seismic displays in this paper follow a polarity convention in which, for a zero-phase wavelet, a positive reflection coefficient is represented by a central trough (plotted white on a variable-density display).

Borehole Data

We used data from exploration borehole AT-8 #1 ST, which was drilled in 1997 in the eastern part of the study area (Fig. 2). The borehole penetrated clastic overburden within a supra-salt, *secondary* minibasin, before penetrating the studied weld and terminating in underlying clastic rocks within the underlying, sub-salt, *primary* minibasin (minibasin terminology after Pilcher et al., 2011). Conventional borehole measurements include differential caliper, bulk density, sonic, gamma ray and neutron porosity, which together allowed us to interpret the lithology of the weld, in addition to the sub- and suprasalt strata. Biostratigraphic data were also available in this borehole, allowing us to constrain the age of strata above and below the weld.

METHODOLOGY

Well-to-Seismic Tie and Seismic Interpretation

We mapped three key seismic horizons; (i) base allochthonous salt; (ii) top allochthonous salt; and (iii) top suprasalt mudstone (see below), in addition to the seabed (Figs 3). By mapping base allochthonous salt we were able to identify structural lows at the base of the sheet, which may represent feeders (Fig. 3A; see also Supplementary Material 1) (see Jackson and Hudec, 2017). Mapping top (Fig. 2B) and base (Fig. 2A) salt allowed us to construct a salt isopach (Fig. 2C), from which we identified areas of thin or welded salt. An overburden isopach, generated from our top salt and seabed maps, revealed the location of secondary minibasins and their relationship to the identified salt weld (Fig. 2D).

Well-log Interpretation

We established the thickness and composition of the salt weld via petrophysical analysis of wireline log data (cf. Jackson et al., 2014). We used a combination of logs to broadly differentiate between: (i) relatively coarse-grained, likely sandstone-prone lithologies; (ii) relatively fine-grained, likely

mudstone-dominated lithologies; and (iii) non-clastic lithologies (e.g. evaporites) (Figs 4 and 5) (Rider and Kennedy, 2011). We show that halite is characterised by relatively low GR values (60 - 75 API), low DT values (101 – 125 μs/ft), and low RHOB values (1.99 – 2.11 g.cm^{-3}). The anomalously high DT values for halite, which are more typically 65-75 μs/ft, may reflect poor hole conditions at this level; our interpretation is supported by the pronounced increase in the caliper change values from c. 0.5 inch within the overlying and underlying clastics, to >1 inch within the upper and lower halite (Fig. 4B). Sandstone present above and below the salt is also characterised by low GR values (50 - 70 API), but has moderate DT values (110 – 130 μs/ft) and RHOB values (1.99 – 2.23 g.cm^{-3}). Mudstone is differentiated from sandstone based on its relatively high GR values (50 – 110 API), moderate to high DT values (116 – 130 μs/ft) and RHOB values (2.14 – 2.31 g.cm^{-3}). We used the caliper log to identify poor borehole conditions, which may signify intervals of strata deformed due to flow of salt (left-hand log track in Fig. 4A and B) (cf. Hilchie, 1968; Theys, 1999).

Biostratigraphic Analysis

We calibrated biostratigraphic data from AT-8 #1 ST (Fig. 6; see also Supplementary Material 2) to the biostratigraphic chart of the Gulf of Mexico Offshore Region, provided by the Bureau of Ocean Energy Management, Regulation and Enforcement from the United States Department of Interior (https://www.data.boem.gov/Paleo/Files/biochart.pdf; webpage accessed 15th November 2017; see also Supplementary Material 3). This chart covers regional and local markers, foraminiferal, planktonic and benthic markers, in addition to regional and local calcareous nannoplanktonic markers, spanning the Jurassic to Quaternary.

SEISMIC ANALYSIS OF THE SALT-TECTONIC STRUCTURE

Here we provide a brief description of the salt-tectonic structure of the study area and the structural context of the weld, focusing on three main structural units: (i) sub-salt minibasins; (ii) allochthonous salt; and (iii) supra-salt minibasins.

Sub-salt Minibasins

Due to migration noise and residual multiples generated by overlying allochthonous salt, sub-salt minibasins are not well imaged in our seismic data. Locally, however, where overlying salt is relatively thin, we observe relatively continuous, variable amplitude, sub-horizontal to gently dipping reflections (Fig. 3). These reflections are truncated below allochthonous salt (or its equivalent weld; see below) across a base salt unconformity that is typically steepest near inferred feeders (labelled ‘F’ in Fig. 3; see also below). In the northeastern part of the study area, immediately north of AT-8 #1 ST, gently south-

dipping strata within a sub-salt minibasin are truncated northward below more steeply dipping strata in a secondary minibasin; we interpret the contact between these two minibasins as a secondary weld (labelled 'S' in Fig. 3E) (*sensu* Jackson and Cramez, 1989). AT-8 #1 ST penetrates the upper c. 1832 m of a sub-salt minibasin beneath supra-salt minibasin 5; well-log (Fig. 4) and biostratigraphic (Fig. 6) data (Fig. 4) indicate the sub-salt basin contains a conformable succession of Late Miocene (Messinian) to Late Pliocene (Gelasian) deep-water clastics.

Allochthonous Salt

Several allochthonous salt bodies are present within the study area. The tops and bases of these bodies are characterised by regionally mappable, high-amplitude peak (positive) and trough (negative) reflections, respectively. The salt is itself characterised by very chaotic, low-amplitude reflections (Figs 3 and 7). The main allochthonous salt body is up to 5500 m thick, broadly U-shaped within the area imaged by our seismic data, and encircles at least the southern end of the minibasin penetrated by AT-8 #1 ST (Fig. 2C). Base salt is very rugose, being defined by at least five sub-circular structural lows that are up to 8 km in diameter and with up to 2 km of relief (Figs 2A and 3); although subsalt seismic imaging is poor, based on (i) their geometric similarity to features observed elsewhere in the Gulf of Mexico (e.g. Pilcher et al., 2011); (ii) their development at the base of a large allochthonous salt body; and (iii) their development adjacent to clearly truncated sub-salt strata, we interpret these features as the tops of diapiric feeders that rose from autochthonous levels, between and thus defining the sub-salt minibasins, and which fed the overlying allochthonous salt canopy (Jackson and Hudec, 2017). Allochthonous salt appears to be locally welded beneath the northern part of minibasin 5 (Fig. 2D); we describe the geophysical expression, and thickness and composition of this weld below. Apart from an anomalous, biostratigraphically defined age-relationship immediately above it (see detailed description below), the salt is immediately underlain and overlain by Early Pleistocene (Gelasian) strata, constraining sheet emplacement to this time (Fig. 6).

Supra-salt Minibasins

At least five supra-salt minibasins, which are up to 12 km wide and 6.5 km thick, overlie the allochthonous salt (i.e. minibasins 1-5) or its equivalent tertiary weld (i.e. northern part of minibasin 5) (see labels in Fig. 2D). Biostratigraphic data indicate an overall downward increase in sediment age within minibasin 5, with Holocene strata passing downwards into earliest Pleistocene (Gelasian) strata (Fig. 6). However, we note an anomalous age-depth relationship in the interval 4359-4394 m, just above the salt weld described more below. Here, a c. 34 m thick interval of anomalously old, Zanclean (4377 and 4394 m) to Piacenzian (4359 m) strata, which is logically overlain by younger, Gelasian strata, is also *underlain*, beneath the weld, by younger, Gelasian strata (e.g. samples at 4526 and 4599 m) (Fig.

6). The significance of this anomalous age-depth relationship is discussed further below in the context of the temporal evolution of the studied weld.

BOREHOLE EXPRESSION OF THE WELD AND SUPERJACENT STRATA

A salt weld, which we will later show is 'apparent', at least where penetrated, (terminology after Wagner and Jackson, 2011; see also Jackson et al., 2014), is developed in the east-central part of the study area, beneath minibasin 5 (Fig. 2E, 3B and E). The weld is defined by two closely spaced seismic reflections, the uppermost being a positive (white) event defining a downward increase in impedance; this seismic response is consistent with acoustically soft, clastic-dominated sedimentary rocks in supra-salt minibasin overlying acoustically harder, evaporite-dominated rocks within the weld (Fig. 7; see also P-wave log in Fig. 4 and data in Fig. 5). Immediately adjacent to AT-8 #1 ST, the weld dips *c*. 28° southward and is thus conformable with underlying and overlying, broadly south-dipping reflections (Figs 3E and 6B). Directly below the weld, a c. 180 m thick package of relatively discontinuous, locally chaotic reflections is present, which is underlain by more continuous reflections (Fig. 7). North of AT-8 #1 ST, the weld dips northward, ultimately connecting to a moderately northward-dipping (*c*. 30°) secondary weld separating two primary minibasins (labelled 'S' in Figs 3E and 7B). East and west of AT-8 #1 ST, the weld connects to the two allochthonous salt bodies (Fig. 3B).

AT-8 #1 ST penetrates the central part of minibasin 5 and its underlying weld (Figs 2E, 3B, 3E, and 7). Well-log data allow us constrain the petrophysical expression, thickness and composition of the weld at this position (Fig. 4). At the approximate depth of the weld, as defined by our seismic mapping, and tied to well control using a regional anisotropy-depth function for correction of seismic depths to well depths, well log data indicate two anomalously low density, high neutron, low gamma ray intervals are present, separated by a 4 m thick mudstone (4412–4436 m; Fig. 4B). These upper and lower, anomalously low-density intervals, which are 5 m and 15 m thick respectively, plot toward the top-left of a standard neutron–density crossplot (the purple and pink points in Fig. 5), thus are petrophysically and, we infer below, compositionally distinct from the over- and underlying, clastic-dominated sequences. We also observe significant increases in the resistivity log measurements in these intervals (4–16 ohm.m; Fig. 4B), in addition to a relative increase in the 'change in caliper' measurement, which implies a 'softer' lithology that caused enlargement of the borehole during drilling (between 4412–4416 and 4425–4436 m; Fig. 4B).

Based on its well log signature, in addition our understanding of the broader salt-tectonic framework of the northern Gulf of Mexico, we interpret the petrophysically distinct intervals encountered between 4412-4436 m contain halite. An alternative interpretation is these intervals represent gas-bearing clastic rocks; however, we dismiss this interpretation based on the absence of gas indicators at deeper or

shallower levels within the borehole. It is important to note that no biostratigraphic data were recovered in this interval, thus the age of the intra-weld mudstone is unknown.

Our petrophysical analysis indicates the *c*. 180 m thick package of discontinuous seismic reflections directly below the weld is mudstone-dominated, having similar petrophysical characteristics to shallow and deeper mudstones (i.e. relatively high gamma-ray, high density and moderate porosity; Figs 4 and 5).

INTERPRETATION AND DISCUSSION

Salt-tectonic context of the weld

The studied salt weld forms part of a regionally extensive salt canopy sourced from deep (Jurassic) Louann salt, lying within the 'amalgamated salt-stock-canopy province' of Pilcher et al. 2011 (Fig. 1B). Previous regional studies suggest canopy emplacement in Atwater Valley occurred during the Middle to Late Miocene, most likely in response to regional shortening and the extrusion of salt from diapiric feeders (Peel et al., 1995). However, our new data, more specifically our observation that the weld and laterally equivalent canopy of inflated salt overlie Early Pleistocene (Gelasian) strata (Fig. 6), suggest canopy emplacement, at least in this part of Atwater Valley, was considerably later (i.e. Early Pleistocene). The difference in timing of canopy emplacement as suggested by Peel et al. (1995) and presented here may reflect: (i) our access to higher-quality seismic reflection and biostratigraphic data, with the latter in particular providing tighter age constraints on the age of sub- and suprasalt strata; and (ii) the fact that canopy emplacement is indeed protracted, with initial diapir breakout and spreading occurring in some areas during the Middle to Late Miocene, but with the canopy not reaching our study area until the Early Pleistocene, several millions years later.

In detail, the age-depth relationship associated with the weld, where Zanclean (early Pliocene) and Piacenzian (late Pliocene) strata just above the weld are encased in younger, Early Pleistocene (Gelasian) strata, is anomalous (Fig. 6). In the absence of a salt weld and its laterally adjacent sheets, we might simply interpret this age inversion to indicate erosion and redeposition of Pliocene strata within younger Pleistocene strata. However, given its structural and stratigraphic association with allochthonous salt, we can refine this interpretation and suggest the Pliocene strata were initially deposited as part of a thin roof capping the canopy, during and after break-out from one or more of its feeders, before being eroded and redeposited within younger Pleistocene strata.

The age and origin of the 4 m thick, intra-weld mudstone, which, despite being thin, accounts for 17% of the total weld fill, may also be explained by a similar mechanism to that responsible for the supra-

297 weld age inversion. In this case, the mudstone initially represented relatively young (i.e. Pliocene)
298 'carapace' material carried atop an advancing salt sheet, later being trapped as the sheet welded. The
299 mudstone was then been overridden by salt from the same or different sheet, which then itself thinned
300 and welded. An alternative interpretation is that the mudstone is much older. For example, it could be
301 the same age as the salt (i.e. Jurassic), having ascended from autochthonous levels within a feeder before
302 being reworked from atop or trapped within an advancing salt sheet that eventually welded.
303
304 **The geophysical and geological expression of salt welds**
305
306 We have shown that good quality seismic reflection data can constrain the gross position of a
307 subhorizontal tertiary salt weld. Seismic data alone do not, however, constrain the completeness or
308 composition of the weld studied here, with borehole data indicating a few tens of metres of halite-
309 dominated stratigraphy (cf. Jackson et al., 2014). Interpreting a complete weld, or the composition of
310 an incomplete weld may, therefore, be extremely challenging in the absence of borehole data;
311 incomplete welds might be erroneously interpreted as being complete, when in reality, a thin veneer of
312 impermeable rock remains between adjacent country rocks. The results of our study support the
313 recommendation of Jackson et al. (2014), who suggested that, until borehole data unequivocally
314 demonstrate the absence of evaporite between flanking strata, the term 'apparent weld' be used to
315 describe seismically defined welds.
316
317 Our observation that a c. 20 m thick sequences remains in the Atwater Valley salt weld is consistent
318 with the predictions of analytical and numerical models presented by Wagner and Jackson (2011),
319 which suggest natural salt welds formed by viscous flow alone may contain anywhere from $\ll$1 m to
320 up to c. 50 m of remnant salt. Our data, and that from the Campos (Wagner and Jackson, 2011) and
321 Santos basins (Jackson et al., 2014), thus support the hypothesis of Wagner and Jackson (2011) that
322 viscous flow is a good analytical approximation of the physical processes occurring during salt thinning
323 and welding, but that viscous flow alone is unlikely to result in complete evacuation of a salt layer.
324 However, it is important to note that a borehole, irrespective of the quantity and quality of data it
325 provides, is only a 1D sample point; it is possible that, away from this sample point, the weld may be
326 locally complete.
327
328 **Composition of salt welds**
329
330 Our borehole data indicate the incomplete tertiary weld penetrated by AT-8 #1 ST is dominated by
331 halite, and that other evaporite (e.g. anhydrite, potash salts) and non-evaporite lithologies, such as
332 carbonate, are absent (Figs 4 and 5). The composition of the weld differs strongly to that encountered
333 in primary welds in the other salt-bearing sedimentary basins. For example, the Parati Weld, Santos

Basin, offshore SE Brazil, which is 22 m thick, is halite-poor, being dominated by carbonate (40%) and anhydrite (40%), with minor amounts of sandstone (16%) and marl (4%). Similarly, halite-poor sequences are observed in incomplete primary welds penetrated by boreholes in the Campos Basin, offshore Brazil (see fig. 17 in Wagner and Jackson, 2011). In that location, 75 boreholes have penetrated multi-layered evaporites in the Retiro Member of the Lagoa Feia Formation (Aptian) (or its nonmarine equivalent). Forty-one of these boreholes penetrate evaporite-bearing sequences that are <100 m thick; of these, only 10 boreholes contain halite and anhydrite, with the remaining 31 boreholes containing only anhydrite.

The compositional variability encountered in salt welds may reflect several factors, such as compositional variations in the autochthonous salt or preferential dissolution of more soluble salts (e.g. halite and bittern salts). For example, autochthonous salt comprising solely halite will yield only halite welds, regardless of structural position within the salt-tectonic system (e.g. primary, secondary and tertiary). Such a case has been informally proposed for the Gulf of Mexico. However, in cases where the autochthonous salt is demonstrably heterogeneous, variations in weld composition may instead reflect a rheological and, ultimately, compositional control on the rate and degree of expulsion of different lithologies during salt thinning. For example, low viscosity, more mobile lithologies, such as halite and potash salt, occurring in thick autochthonous salt in sufficiently large quantities, may be preferentially expelled from thinning salt before relatively high viscosity, less mobile lithologies, such as carbonate, anhydrite and sandstone. As such, during welding, salt becomes relatively enriched in these less mobile, non-halite/potash salt lithologies, which, due to the effects of boundary drag along the upper and low salt contacts, becomes trapped in the weld as the salt thinned (compare 'differential purification by movement'; Kupfer, 1968; see also Wagner and Jackson, 2011 and Jackson et al., 2014). Salt structures flanking welds, be they diapirs or autochthonous bodies, should thus be relatively enriched in mobile halite and potash salts, and lack non-halite lithologies; this hypothesis is directly proven by borehole data (Jackson et al., 2014; 2015), and at least given some indirect support from seismic facies analysis (Van Gent et al., 2011; Fiduk and Rowan, 2012; Strozyk et al., 2012).

The differential purification by movement model, which only applies to compositionally heterogeneous systems, suggests increasing compositional fractionation of salt should occur as the salt-tectonic system evolves; more viscous, less mobile, and/or denser units are typically stranded within the autochthonous level, trapped in primary welds, or stranded near the basal root of diapirs, whereas less viscous and/or less dense units form the cores of these diapirs and, potentially, genetically related, allochthonous sheets and canopies. As such, supra-sheet minibasins forming above allochthonous salt sheets or canopies should subside into 'purer' salt dominated by halite and potash salts and, accordingly, underlying tertiary welds should be relatively rich in these rock types. Our data support this model, with a halite-rich weld being observed at relatively shallow levels in this salt-tectonic system. However, due to a lack

of deep borehole data and post-depositional salt flow, we do not know the composition of autochthonous salt in the Gulf of Mexico, thus we cannot prove the halite-rich nature of the weld described here simply reflects strain-induced compositional fractionation.

Observations from exposed salt-tectonic systems show that the structurally shallow levels of some diapirs may contain very large (i.e. up to several kilometres in diameter) clasts of rock clearly denser than the encasing salt (e.g. igneous rock, anhydrite; Dalgano and Johnson, 1968; Kent, 1979; Richter-Bernberg, 1980; Gansser, 1992; Lawton and Amato, 2017). These clasts were carried up several kilometres from autochthonous levels within the rising salt and have not yet sunk, with numerical and physical models indicating this occurs because salt rise rate exceeds the descent rate of the denser clast (e.g. Koyi & Schott, 2000; Koyi, 2001; Chemia et al., 2008). Observations from natural examples, and numerical and physical models thus challenge the 'differential purification by movement' model, showing that rheology alone may not control vertical changes in composition within salt-tectonics systems. More specifically, numerical models suggest that sedimentation rate, salt viscosity, diapir width, and stratigraphic position of the dense layer within the initial autochthonous layer may also control the ability of rising salt to entrain, transport, and suspend relatively dense clasts (Chemia et al., 2008).

Implications for petroleum systems development in salt basins

This observation, along with the fact that various lithologies may remain in an incomplete weld, may directly impact hydrocarbon prospectivity in salt-tectonic basins. For example, the sealing capacity of an incomplete weld containing very low-permeability halite is likely to be higher than an incomplete weld containing permeable layers of carbonates and clastics. We may therefore speculate that primary welds, which may contain relatively little low-permeability halite and thus higher proportions of more permeable non-evaporitic lithologies, may be poorer seals and thus more susceptible to leakage. Additional data from primary, secondary, and tertiary welds, in addition to information on the hydrocarbon presence (or absence) in sub-salt strata, is required to test this hypothesis.

CONCLUSIONS

3D isotropic Kirchhoff prestack depth migrated (KPSDM) seismic data image the salt-tectonic structure and reveal the geophysical expression of a tertiary salt weld in the Atwater Valley protraction area of the Gulf of Mexico. This weld formed at the base of a Plio-Pleistocene minibasin that subsided into a thick allochthonous salt canopy fed by several diapiric feeders. Seismic reflection data suggest the weld is devoid of salt and is thus 'complete', although borehole data demonstrate the weld is in fact 'incomplete', being *c*. 24 m thick and containing an upper 5 m thick halite and a lower 15 m thick halite,

separated by a 4 m thick mudstone. The origin and age of the intra-weld mudstone is unclear; it may be Late Jurassic, representing material transported upwards from the autochthonous level within a feeder, or Pliocene, representing carapace material incorporated into the canopy prior to thinning and welding. We show that even relatively modern 3D seismic reflection data may not resolve salt weld thickness, with the presence of a relatively thin layer of salt supporting analytically derived models of welding based on viscous flow. Furthermore, the halite-dominated character of the weld supports the hypothesis that tectonic purification occurs during flow of salt from autochthonous to allochthonous levels. In terms of hydrocarbon exploration, understanding the thickness and composition of material left in salt welds is important, with data presented here and in other studies suggesting that, for the same given thickness, the seal potential of tertiary welds may be higher than that of primary (or secondary) welds due to them being relatively enriched in low-permeability halite.

ACKNOWLEDGEMENTS

We thank Petroleum Geo-Services (PGS) for permission to use and show their proprietary seismic data, and Schlumberger for providing Petrel software to Imperial College via an Academic License Agreement. Biostratigraphic data for the AT-8 #1 ST were provided by Lexco Data Systems, L. P. in conjunction with Petroleum Geo-Services (PGS). Thomas Hearon and two anonymous reviewers are thanked for helpful comments that helped improve the final manuscript. We also thank Bruce Trudgill for his editorial handling, as well as Mike Hudec, Yikuo Liu, and Connor O'Sullivan for very helpful discussions during the course of this study.

REFERENCES

Chemia, Z., Koyi, H., and Schmeling, H, 2008, Numerical modelling of rise and fall of a dense layer in salt diapirs: Geophysical Journal International, 172, 798–816.

Cohen, H.A., Hardy, S., 1996. Numerical modelling of stratal architectures resulting from differential loading of a mobile substrate, in G.I. Alsop, D.J. Blundell, and I. Davison, eds., Salt tectonics: Geological Society London Special Publications, 100, 265–273.

Dalgarno, C.R., and Johnson, J.E., 1968, Diapiric structures and late Precambrian-Early Cambrian sedimentation in the Flinders Ranges, South Australia: American Association of Petroleum Geologists Memoir, 8, 301–314.

Diegel, F. A., J. F. Karlo, D. C. Schuster, R. C. Shoup, and P.R. Tauvers, 1995, Cenozoic structural evolution and tectono-stratigraphic framework of the northern Gulf Coast continental margin, in M. P.

445 A. Jackson, D. G. Roberts, and S. Snelson, eds., Salt tectonics: A global perspective: AAPG Memoir
446 65, 109–151.
447
448 Fiduk, J.C., and M.G. Rowan, 2012, Analysis of folding and deformation within layered evaporites in
449 Blocks BM-S-8 & -9, Santos Basin, Brazil, in G.I. Alsop, S.G. Archer, A.J. Hartley, N.T. Grant, and R.
450 Hodgkinson, eds., Salt tectonics, sediments and prospectivity: Geological Society of London Special
451 Publications, 363, 471-487.
452
453 Gansser, A., 1992, The enigma of the Persian salt-dome inclusions: Eclogae Geologicae Helvetiae, 85,
454 825–846.
455
456 Hazzard, R. T., W. C. Spooner, and B. W. Blanpied, 1947, Notes on the stratigraphy of the formations
457 which underlie the Smackover Limestone in south Arkansas, northeast Texas, and north Louisiana:
458 Shreveport Geological Society, Reference Report on Certain Oil and Gas Fields of North Louisiana,
459 South Arkansas, Mississippi and Alabama, vol. II, 483–503.
460
461 Herron, D.A., 2011. First steps in seismic interpretation. Society of Exploration Geophysicists.
462
463 Hilchie, D.W. (1968). Caliper Logging – theory and practice. The Log Analyst, 9 (1), p. 3-12.
464
465 Hoetz, G., J. Steenbrinkl, N. Bekkers, A. Vogelaar, and S. Luthi, 2011, Salt-induced stress anomalies:
466 an explanation for variations in seismic velocity and reservoir quality: Petroleum Geoscience, 17, 385-
467 396.
468
469 Hudec, M.R., and M.P.A. Jackson, 2007, Terra infirm: understanding salt tectonics: Earth-Science
470 Reviews, 82, 1-28.
471
472 Hudec, M. R., M. P. A. Jackson, and F. J. Peel, 2013a, Influence of deep Louann structure on the
473 evolution of the northern Gulf of Mexico: AAPG Bulletin, 97, 1711–1735.
474
475 Hudec, M. R., I. O. Norton, M. P. A. Jackson, and F. J. Peel, 2013b, Jurassic evolution of the Gulf of
476 Mexico salt basin: AAPG Bulletin, 97, 1683–1710.
477
478 Humphris, C. C., Jr., 1978, Salt movement on continental slope, northern Gulf of Mexico, in A. H.
479 Bouma, G. T. Moore, and J. M. Coleman, eds., Framework, facies, and oil-trapping characteristics of
480 the upper continental margin: AAPG, vol. 7, of, Studies in Geology, 69–86.
481

Jackson, C.A-L, Rodriguez, C.R., Rotevatn, A., and Bell R.E., 2014, Geological and geophysical expression of a primary salt weld: An example from the Santos Basin, Brazil: Interpretation, Vol: 2, Pages: SM77-SM89.

Jackson, C.A-L., Jackson, M.P.A., Hudec, M.R., and Rodriguez, C.R., 2015, Enigmatic structures within salt walls of the Santos Basin—Part 1: Geometry and kinematics from 3D seismic reflection and well data. Journal of Structural Geology, 75, 135-162.

Jackson, M.P.A., and C. Cramez, 1989, Seismic recognition of salt welds in salt tectonic regimes: Proceedings of the GCSSEPM Foundation 10th Annual Bob F. Perkins Research Conference, 66-71.

Jackson, M.P.A., and Hudec, M.R., 2017. Salt Tectonics: Principles and Practice. Cambridge University Press.

Kent, P.E., 1979, The emergent Hormuz salt plugs of southern Iran: Journal of Petroleum Geology, 2, 117–144.

Koyi, H., 2001, Modeling the influence of sinking anhydrite blocks on salt diapirs targeted for hazardous waste disposal: Geology, 29, 387–390.

Koyi, H., and Schott, B., 2000, The rise and fall of denser blocks within salt diapirs: Bollettino di Geofisica teorica ed applicata, 42, 64–66.

Kneller, E.A., and Johnson, C.A., 2011, Plate kinematics of the Gulf of Mexico based on integrated observations from the Central and South Atlantic: Gulf Coast Association of Geological Societies Transactions, 61, 283–300.

Kupfer, D.H., 1968, Relationship of internal and external structure of salt domes. In: J. Braunstein, and G.D. O'Brien, eds., Diapirism and diapirs: AAPG Memoir, 8, 79–89.

Lawton, T.F., and Amato, J.M., (2017) U-Pb ages of igneous xenoliths in a salt diapir, La Popa basin: Implications for salt age in onshore Mexico salt basins: Lithosphere, 9, 745–758.

Liro, L., and S.M. Holdaway, 2011, Salt welds in the deepwater Gulf of Mexico – Uncertainties in the amount of remnant salt: seismic and well examples: AAPG Abstracts with Programs, 986760, p113.

Peel, F. J., C. J. Travis, and J. R. Hossack, 1995, Genetic structural provinces and salt tectonics of the

519 Cenozoic offshore U.S. Gulf of Mexico: A preliminary analysis: AAPG Memoir, 65, 153–175.
520
521 Pilcher, R.S., Kilsdonk, B. and Trude, J., 2011. Primary basins and their boundaries in the deep-water
522 northern Gulf of Mexico: Origin, trap types, and petroleum system implications. AAPG bulletin, 95(2),
523 pp.219-240.
524
525 Pindell, J., and J.F. Dewey, 1982, Permo-Triassic reconstruction of western Pangea and the evolution
526 of the Gulf of Mexico/Caribbean region: Tectonics, 1, 179–211.
527
528 Richter-Bernburg, G., 1980, Salt domes in northwest Germany: Centres de Recherches Exploration-
529 Production, Bulletin, Elf Aquitaine, 4, 373–393.
530
531 Rider, M. and Kennedy, M. (2011). The Geological Interpretation of Well Logs (3rd ed.). Rider-French
532 Consulting Ltd, Scotland.
533
534 Rowan, M.G., 1995, Structural styles and evolution of allochthonous salt, central Louisiana outer shelf
535 and upper slope, in M. P. A. Jackson, D. G. Roberts, and S. Snelson, eds., Salt tectonics: A global
536 perspective: AAPG Memoir 65, 199–228.
537
538 Rowan, M.G., 2004, Do salt welds seal? Proceedings of the GCSSEPM Foundation 24th Annual Bob
539 F. Perkins Research Conference (Salt-Sediment Interactions and Hydrocarbon Prospectivity: Concepts,
540 Applications, and Case Studies for the 21st Century), 390-403.
541
542 Rowan, M.G., Lawton, T.F., Giles, K.A., 2012, Anatomy of an exposed vertical salt weld and flanking
543 strata La Popa Basin, Mexico. in G.I. Alsop, S.G. Archer, A.J. Hartley, N.T. Grant, and R. Hodgkinson,
544 eds., Salt tectonics, sediments and prospectivity: Geological Society of London Special Publications,
545 363, 33-57.
546
547 Salvador, A., 1987, Late Triassic-Jurassic paleogeography and origin of Gulf of Mexico Basin: AAPG
548 Bulletin, 71, 419–451.
549
550 Strozyk, F., H. Van Gent, J.L. Urai, and P.A. Kukla, 2012, 3D seismic study of complex intra-salt
551 deformation: An example from the Upper Permian Zechstein 3 stringer, western Dutch offshore, in G.I.
552 Alsop, S.G. Archer, A.J. Hartley, N.T. Grant, and R. Hodgkinson, eds., Salt tectonics, sediments and
553 prospectivity: Geological Society of London Special Publications, 363, 489-501.
554
555 Theys, P. (1999). Log Data Acquisition and Quality Controls (2nd ed.). Editions Technip, Paris

Van Gent, H., J.L. Urai, and M. de Keijzer, 2011, The internal geometry of salt structures – a first look using 3D seismic data from the Zechstein of the Netherlands: Journal of Structural Geology, 33, 292-311.

Wagner III, B.H., 2010, An analysis of salt welding: Unpublished PhD dissertation, University of Texas at Austin, 218pp.

Wagner III, B.H., and M.P.A. Jackson, 2011, Viscous flow during salt welding: Tectonophysics, 510, 309-326.

FIGURE CAPTIONS

Fig. 1. (A) Simplified map showing the location of the study area. The location of the geoseismic profile (after Pilcher, et al. 2011) shown in Fig. 1B is indicated. (B) Broadly NNW-trending geoseismic profile showing the approximate structural position and tectono-stratigraphic context of the study area. p=primary weld; t=tertiary weld. Note that no secondary welds are shown on this profile. TMM=top Middle Miocene; TPL=top Pliocene. The location of the profile is shown in Fig. 1A. Note that this line lies c. 50 km west of the study area (see Fig. 1A).

Fig. 2. (A) base salt depth map; (B) top salt depth map; (C) salt isopach; (D) post-salt isopach; and (E) a simplified salt-tectonic features map. 1-5 in (D) refers to minibasins described in the text. Locations of mapped seismic horizons shown in (A) and (B) are shown in Fig. 3.

Fig. 3. Broadly E-trending seismic profiles through the (A) north, (B) centre, and (C) south of the study area. Locations of profiles are shown in Fig. 2E. (B) intersects through the studied salt weld and borehole AT-8 #1 ST; (D) Broadly N-trending seismic profiles in the (D) west and (E) east of the study area. (D) and (E) intersects postulated salt feeders (Fig. 2E), with (E) also intersecting the studied salt weld and borehole AT-8 #1 ST. s=secondary weld; t=tertiary weld. The locations of Fig. 6A and B are shown in (B) and (E), respectively.

Fig. 4. (A) Well-log and lithology data from the depth interval 4300-4500 m in AT-8 #1 ST. The entire non-evaporitic sedimentary succession shown here is Upper Pliocene. Note the halite-rich character of the weld. For location of borehole, see Figs 2, 3B and D. (B) Details of the well-log expression of interval 4400-4500 in AT-8 #1 ST. The weld and the main lithological subdivisions are indicated, with the colour-coded text referring to the colours in Fig. 5. The seismic polarity convention used for these seismic profiles and those in Fig. 6 are shown in (A).

Fig. 5. Neutron-density cross-plot of petrophysical data from the depth interval 4300-4500 m in AT-8 #1 ST. Note the distinct expression of intra-weld halite, which is characterised by significantly lower neutron values than underlying or overlying clastics.

Fig. 6. Compilation of biostratigraphic data from borehole AT-8 #1 ST showing the age of sub- and suprasalt strata flanking the studied salt weld. Raw data are shown in Supplementary Material 2, with these data calibrated to the chart shown in Supplementary Material 3.

Fig. 7. (A) N-trending seismic profile (IL44638) through borehole AT-8 #1 ST; (B) E-trending profile (XL6602) through borehole AT-8 #1 ST. Both profiles illustrate the seismic character of the salt weld and adjacent stratigraphy. Note the distinctly chaotic seismic facies directly underlying the weld. The location of (A) is shown in Fig. 3B and the location of (B) in Fig. 3E.

Supplementary Material 1 – Uninterpreted versions of seismic profiles shown in Fig. 3.

Supplementary Material 2 – Table of biostratigraphic data from borehole AT-8 #1 ST. Reports 1-3 are assumed to reflect different analysis of the recovered core material that may, in certain instances, be from the same depth, but which may describe different fauna; e.g. 14310 m in Report 1 (Globoquadrina altispira) and 2 (Globorotalia menardii, coiling change left/right), which both yield an Upper Pliocene age, and 8160 m in Report 1 (Gephyrocapsa aperta acme) and 2 (Stilostomella antillea), which both yield a Lower Pleistocene age.

Supplementary Material 3 – Gulf of Mexico biostratigraphic chart from the Bureau of Ocean Energy Management (BOEM), Regulation and Enforcement from the United States Department of Interior (https://www.data.boem.gov/Paleo/Files/biochart.pdf. Webpage accessed 15th November 2017.

Supplementary Material 4 – Uninterpreted versions of seismic profiles shown in Fig. 7.

Fig. 1

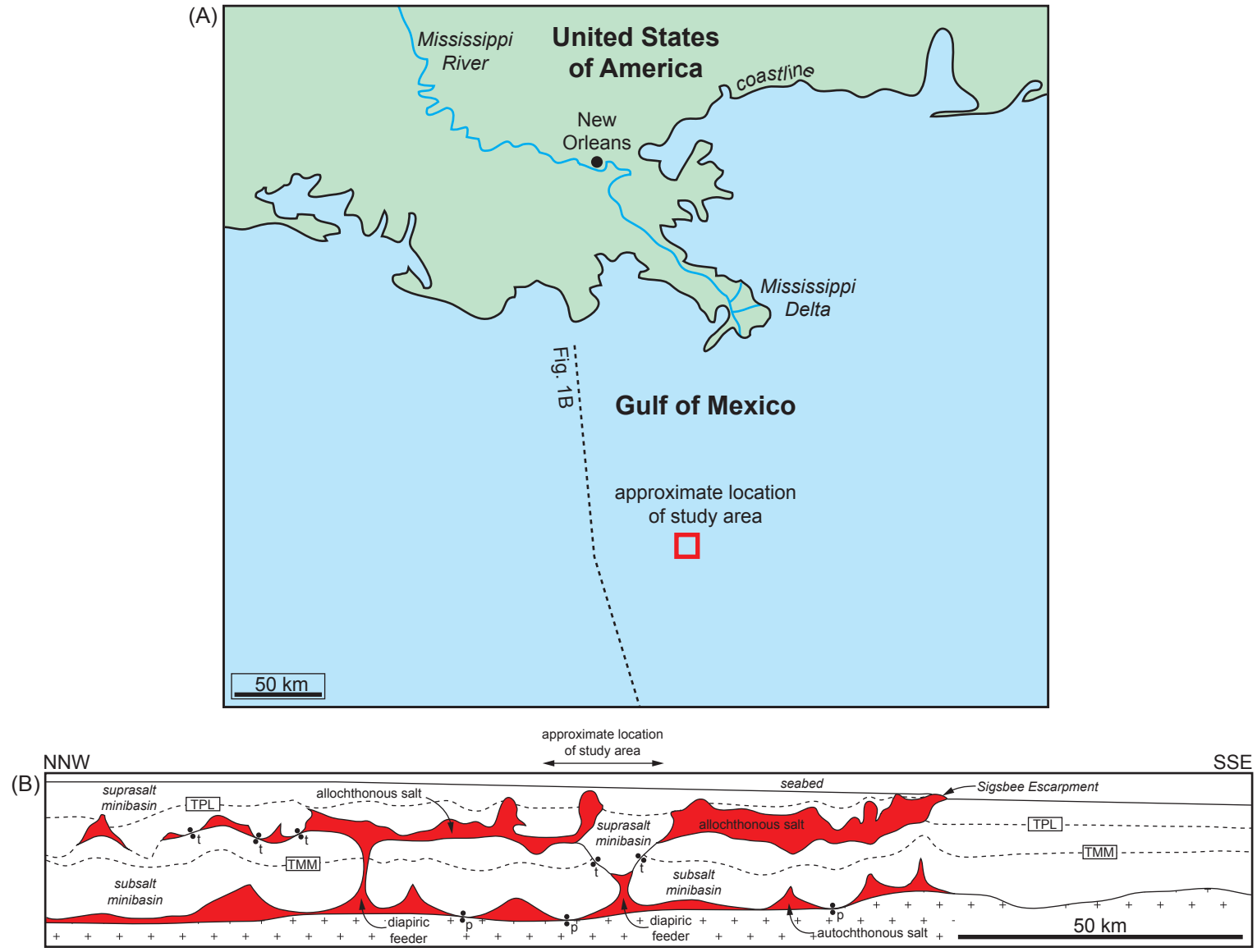
(A)
Mississippi River
United States of America
coastline
New Orleans
Mississippi Delta
Fig. 1B
Gulf of Mexico
approximate location of study area
50 km
approximate location of study area
NNW
SSE
(B)
suprasalt minibasin
TPL
allochthonous salt
seabed
Sigsbee Escarpment
TMM
subsalt minibasin
diapiric feeder
autochthonous salt
50 km

Fig. 2

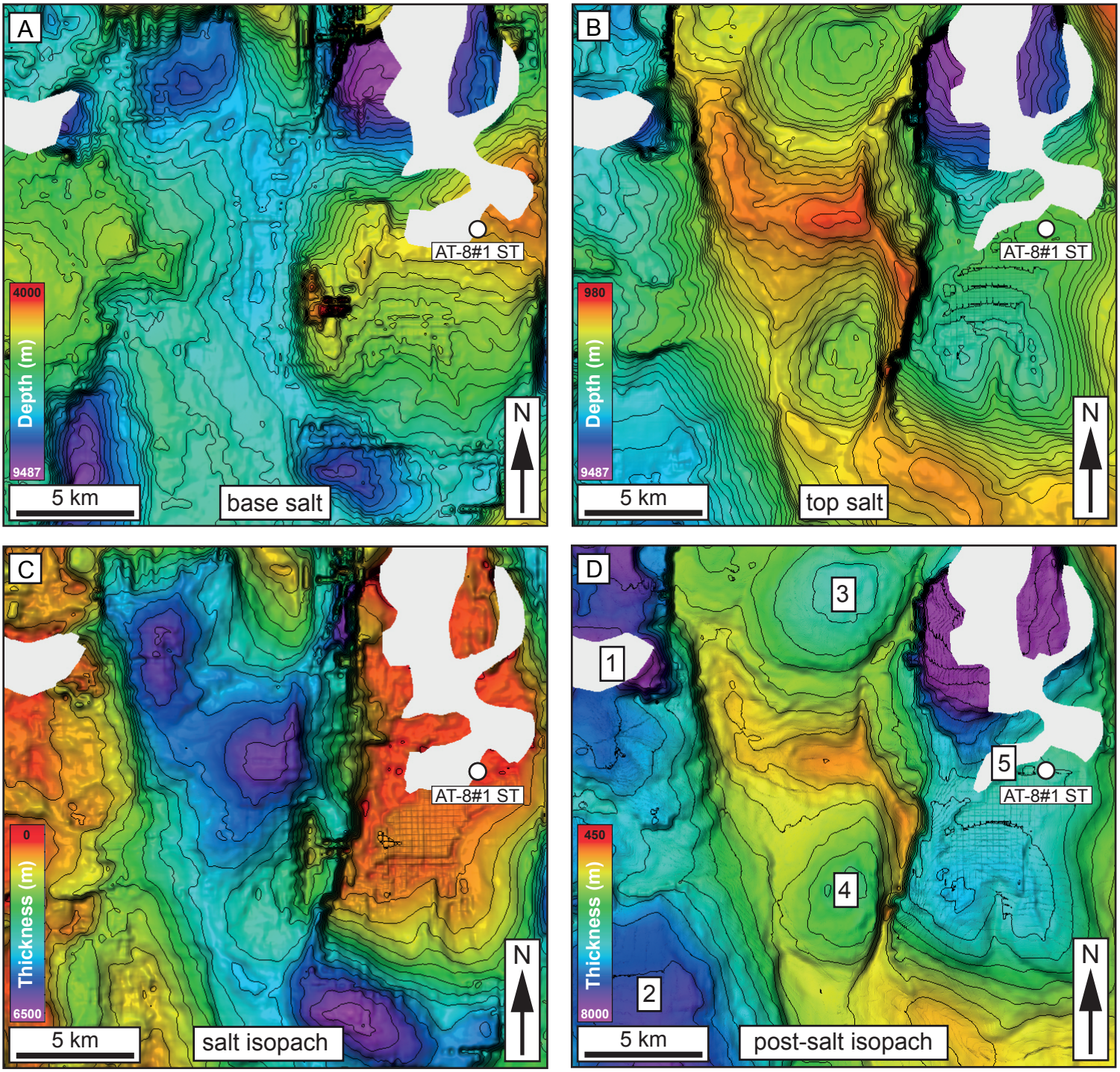
A
AT-8#1 ST
4000
Depth (m)
9487
5 km
base salt
N
B
AT-8#1 ST
980
Depth (m)
9487
5 km
top salt
N
C
AT-8#1 ST
0
Thickness (m)
6500
5 km
salt isopach
N
D
3
1
5
AT-8#1 ST
450
Thickness (m)
4
2
8000
5 km
post-salt isopach
N

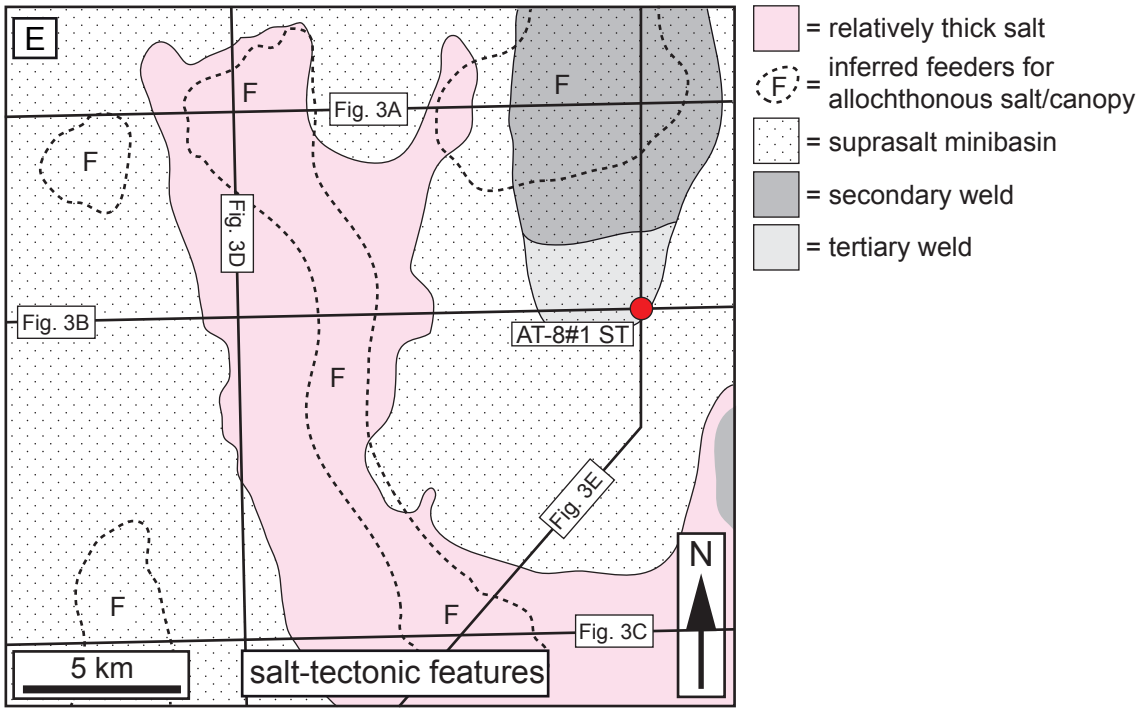
E
F
Fig. 3A
F
F
Fig. 3D
Fig. 3B
AT-8#1 ST
F
Fig. 3E
N
F
F
Fig. 3C
5 km
salt-tectonic features
= relatively thick salt
F = inferred feeders for allochthonous salt/canopy
= suprasalt minibasin
= secondary weld
= tertiary weld

Fig. 3

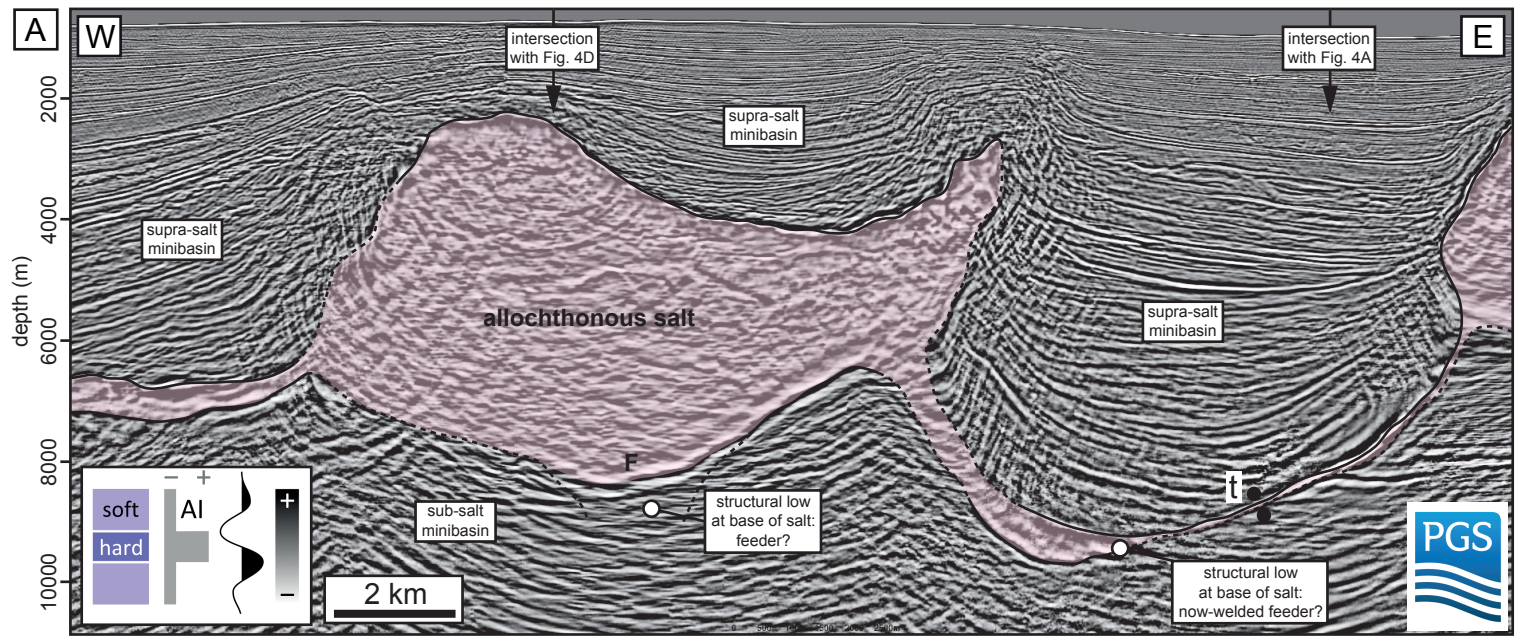
A
W
E
intersection with Fig. 4D
intersection with Fig. 4A
supra-salt minibasin
allochthonous salt
F
t
sub-salt minibasin
structural low at base of salt: feeder?
structural low at base of salt: now-welded feeder?
soft
hard
AI
2 km
depth (m)
2000
4000
6000
8000
10000
PGS

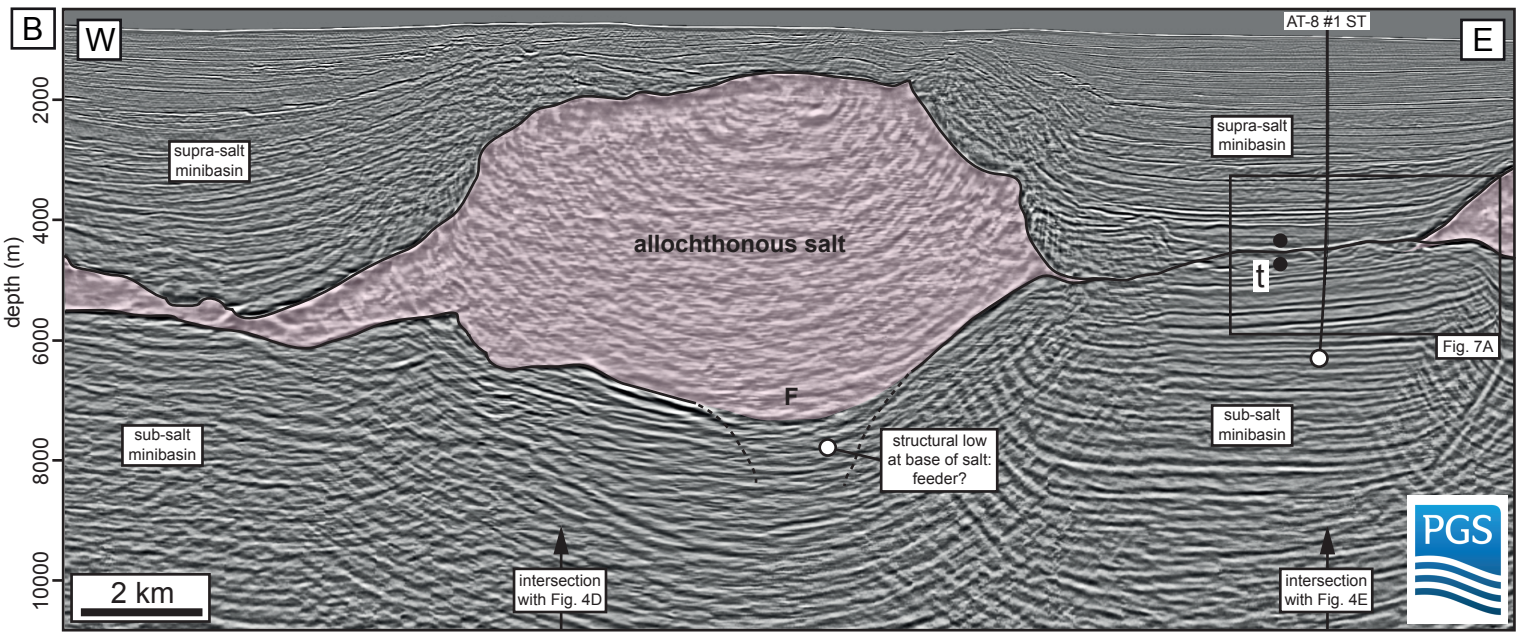
B
W
E
AT-8 #1 ST
supra-salt minibasin
allochthonous salt
t
Fig. 7A
F
sub-salt minibasin
structural low at base of salt: feeder?
intersection with Fig. 4D
intersection with Fig. 4E
2 km
depth (m)
2000
4000
6000
8000
10000
PGS

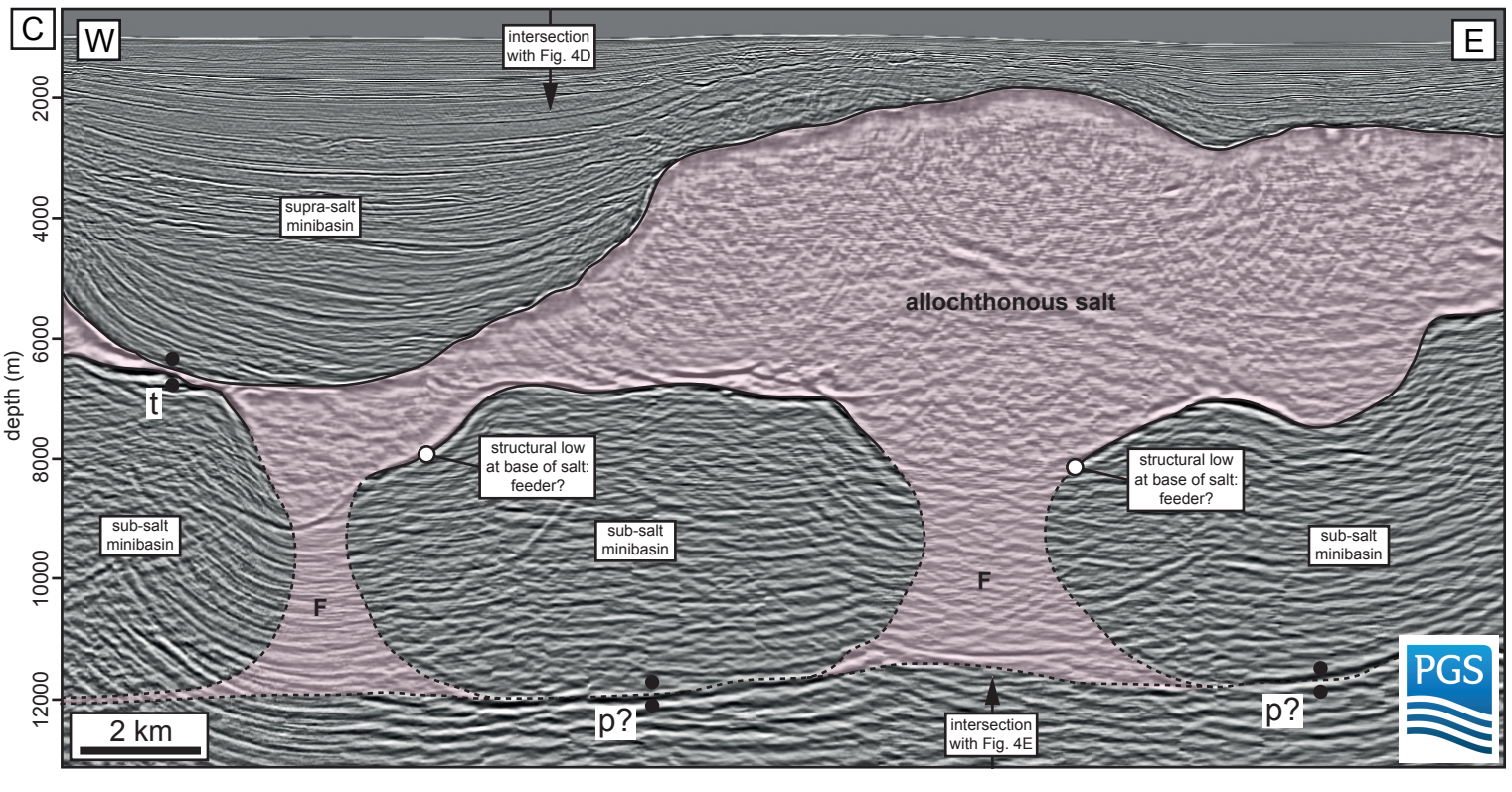
C
W
E
intersection with Fig. 4D
supra-salt minibasin
allochthonous salt
t
structural low at base of salt: feeder?
sub-salt minibasin
F
p?
intersection with Fig. 4E
2 km
depth (m)
2000
4000
6000
8000
10000
12000
PGS

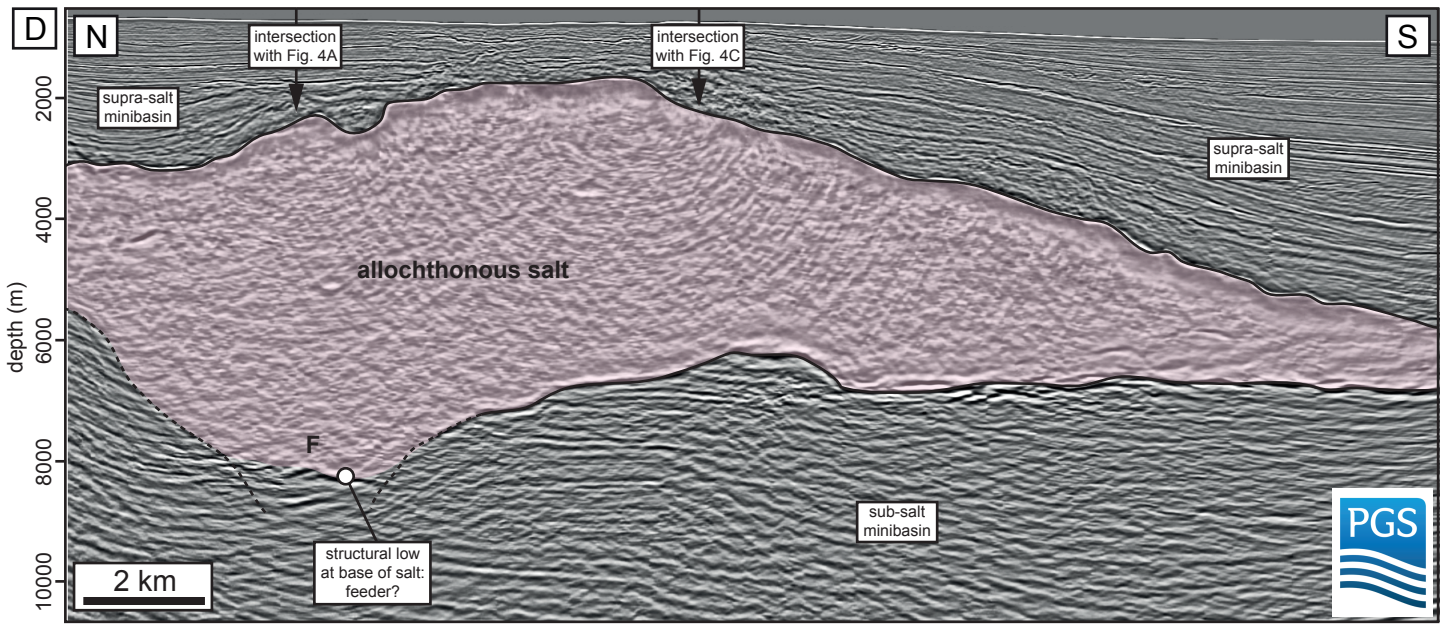
D
N
S
intersection with Fig. 4A
intersection with Fig. 4C
supra-salt minibasin
allochthonous salt
F
structural low at base of salt: feeder?
sub-salt minibasin
2 km
depth (m)
2000
4000
6000
8000
10000
PGS

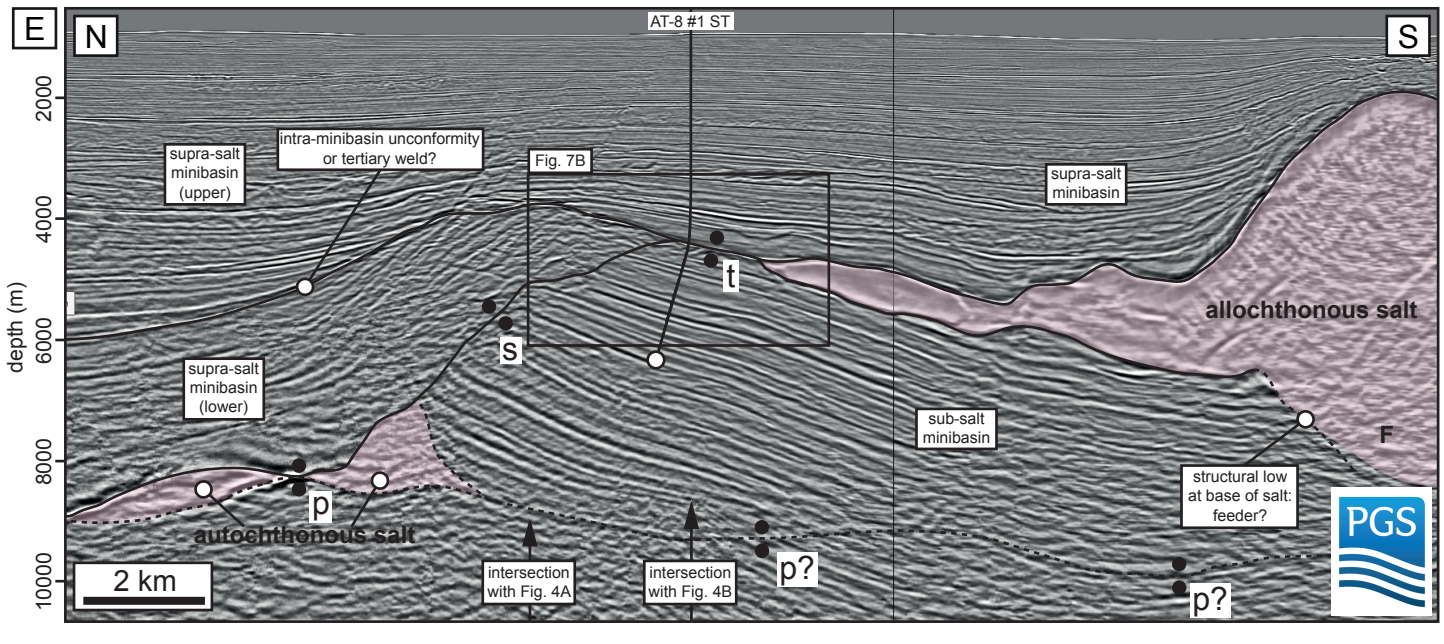
E
N
S
AT-8 #1 ST
intra-minibasin unconformity or tertiary weld?
supra-salt minibasin (upper)
Fig. 7B
supra-salt minibasin
allochthonous salt
t
s
supra-salt minibasin (lower)
sub-salt minibasin
F
structural low at base of salt: feeder?
p
autochthonous salt
intersection with Fig. 4A
intersection with Fig. 4B
p?
2 km
depth (m)
2000
4000
6000
8000
10000
PGS

Fig. 4

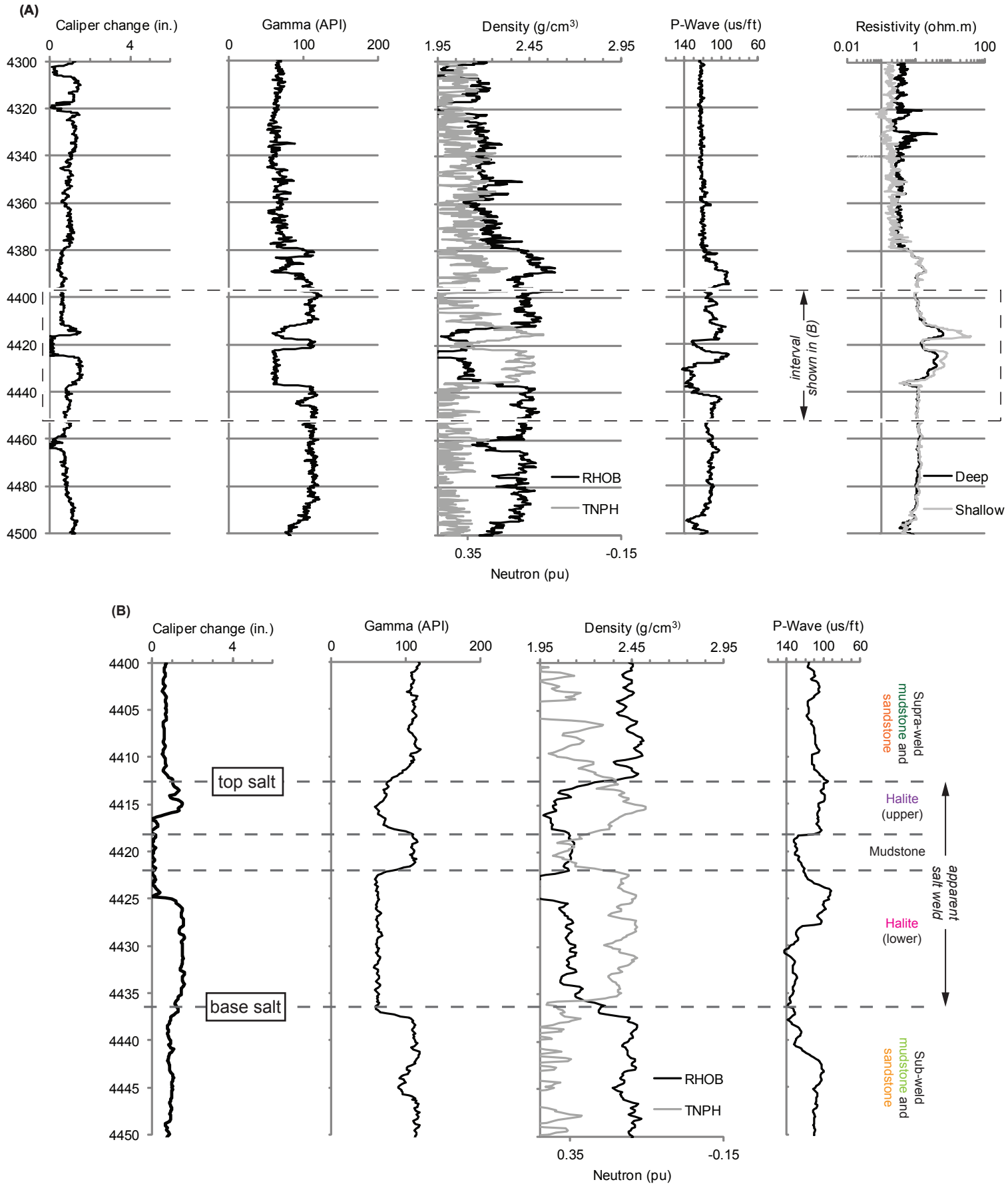
(A)
Caliper change (in.)
0
4
Gamma (API)
0
100
200
Density (g/cm3)
1.95
2.45
2.95
P-Wave (us/ft)
140
100
60
Resistivity (ohm.m)
0.01
1
100
4300
4320
4340
4360
4380
4400
4420
4440
4460
4480
4500
interval shown in (B)
RHOB
TNPH
Deep
Shallow
0.35
-0.15
Neutron (pu)
(B)
Caliper change (in.)
0
4
Gamma (API)
0
100
200
Density (g/cm3)
1.95
2.45
2.95
P-Wave (us/ft)
140
100
60
4400
4405
4410
4415
4420
4425
4430
4435
4440
4445
4450
top salt
base salt
Supra-weld mudstone and sandstone
Halite (upper)
Mudstone
Halite (lower)
Sub-weld mudstone and sandstone
apparent salt weld
RHOB
TNPH
0.35
-0.15
Neutron (pu)

Fig. 5

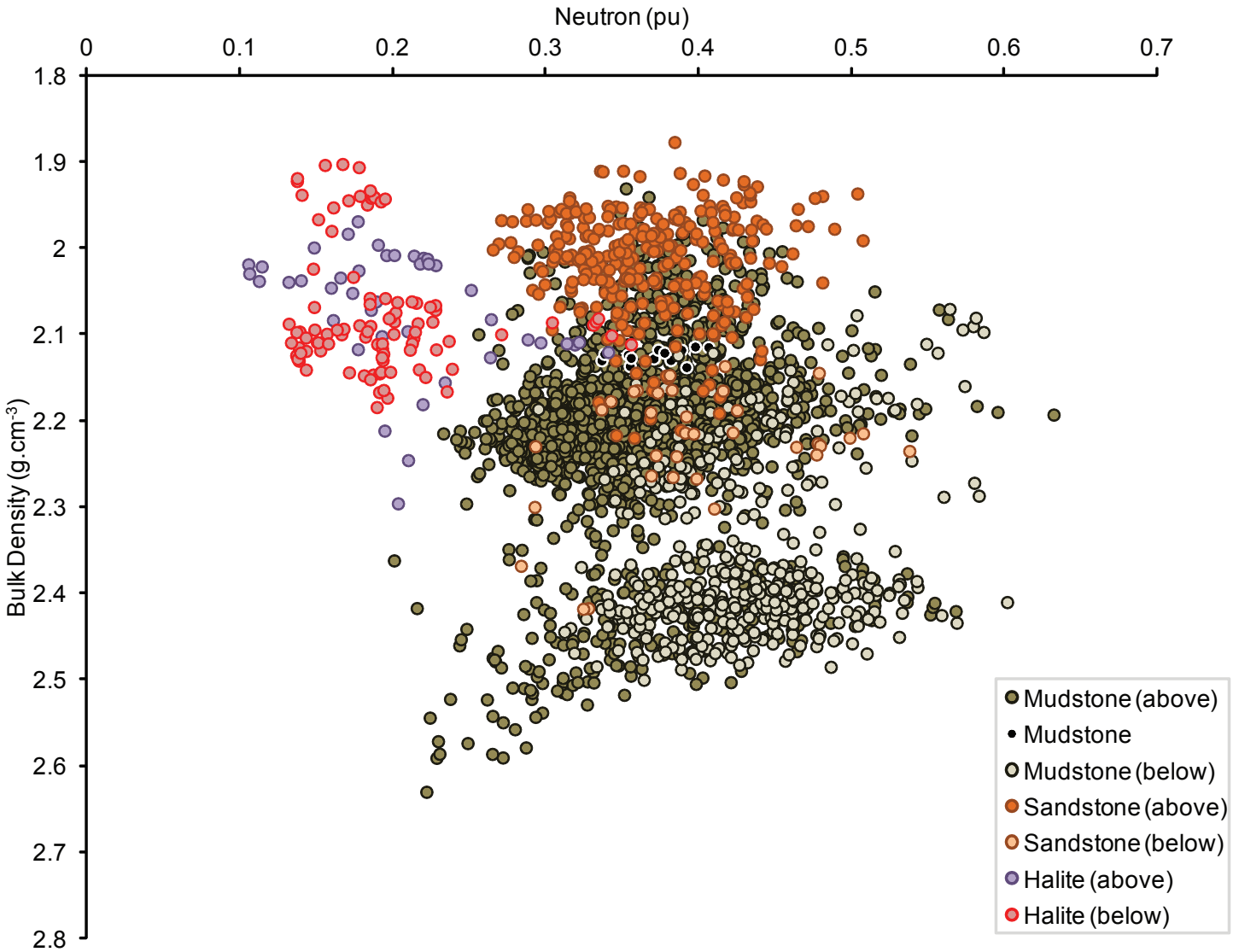
Neutron (pu)
0
0.1
0.2
0.3
0.4
0.5
0.6
0.7
Bulk Density (g.cm-3)
1.8
1.9
2
2.1
2.2
2.3
2.4
2.5
2.6
2.7
2.8
Mudstone (above)
Mudstone
Mudstone (below)
Sandstone (above)
Sandstone (below)
Halite (above)
Halite (below)

Fig. 6

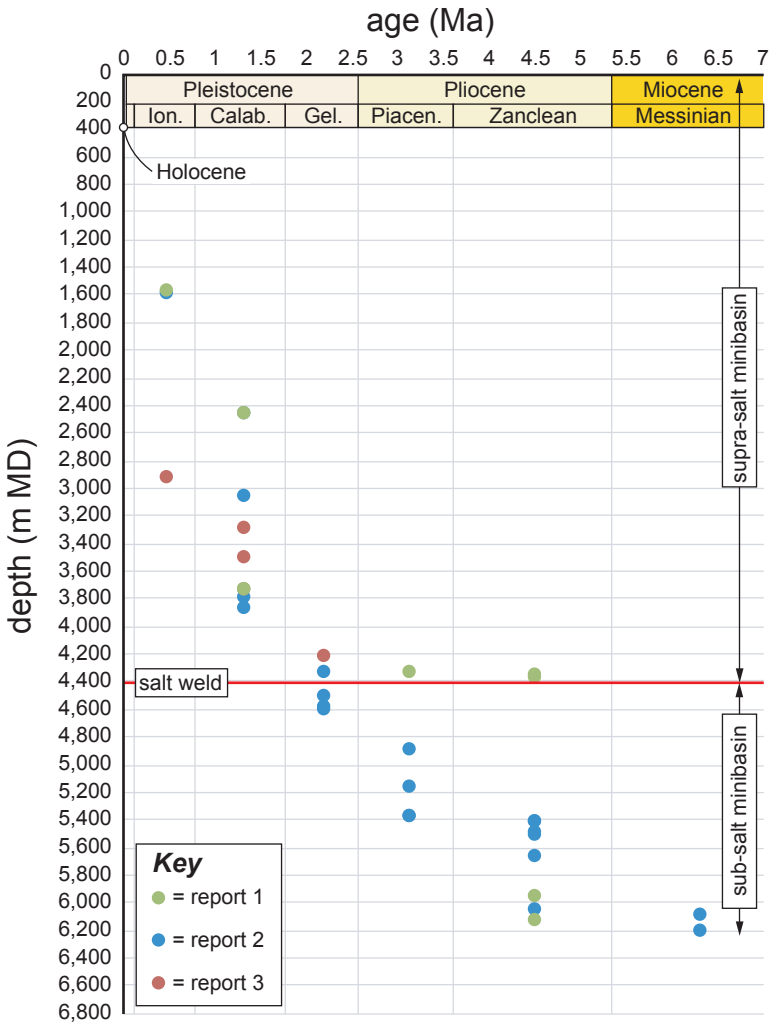
age (Ma)
0 0.5 1 1.5 2 2.5 3 3.5 4 4.5 5 5.5 6 6.5 7
Pleistocene
Pliocene
Miocene
Ion.
Calab.
Gel.
Piacen.
Zanclean
Messinian
Holocene
depth (m MD)
0 200 400 600 800 1,000 1,200 1,400 1,600 1,800 2,000 2,200 2,400 2,600 2,800 3,000 3,200 3,400 3,600 3,800 4,000 4,200 4,400 4,600 4,800 5,000 5,200 5,400 5,600 5,800 6,000 6,200 6,400 6,600 6,800
salt weld
supra-salt minibasin
sub-salt minibasin
Key
= report 1
= report 2
= report 3

Fig. 7

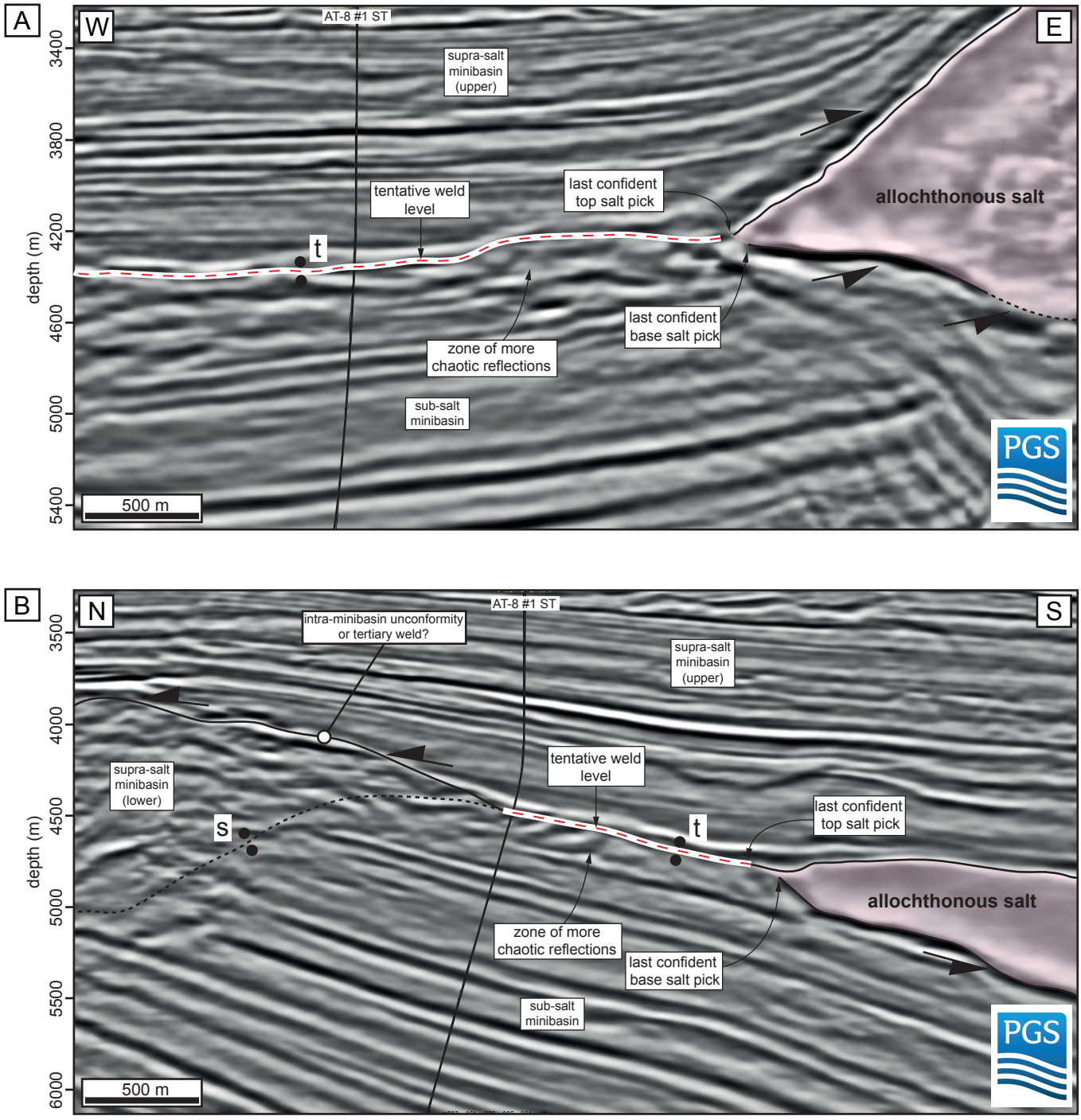
A
W
E
AT-8 #1 ST
supra-salt minibasin (upper)
tentative weld level
last confident top salt pick
allochthonous salt
t
last confident base salt pick
zone of more chaotic reflections
sub-salt minibasin
depth (m)
3400
3800
4200
4600
5000
5400
500 m
PGS
B
N
S
AT-8 #1 ST
intra-minibasin unconformity or tertiary weld?
supra-salt minibasin (upper)
supra-salt minibasin (lower)
tentative weld level
s
t
last confident top salt pick
allochthonous salt
zone of more chaotic reflections
last confident base salt pick
sub-salt minibasin
depth (m)
3500
4000
4500
5000
5500
6000
500 m
PGS

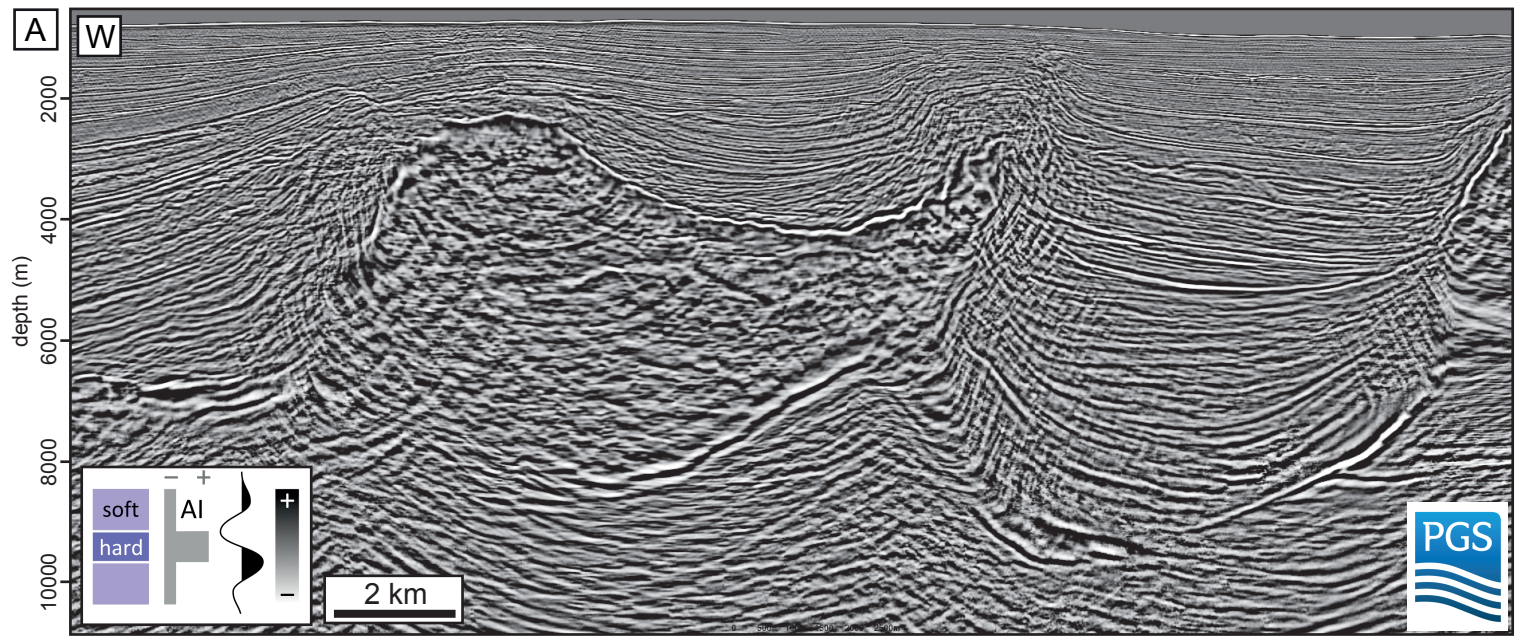
A
W
depth (m)
2000
4000
6000
8000
10000
soft
hard
AI
2 km
PGS

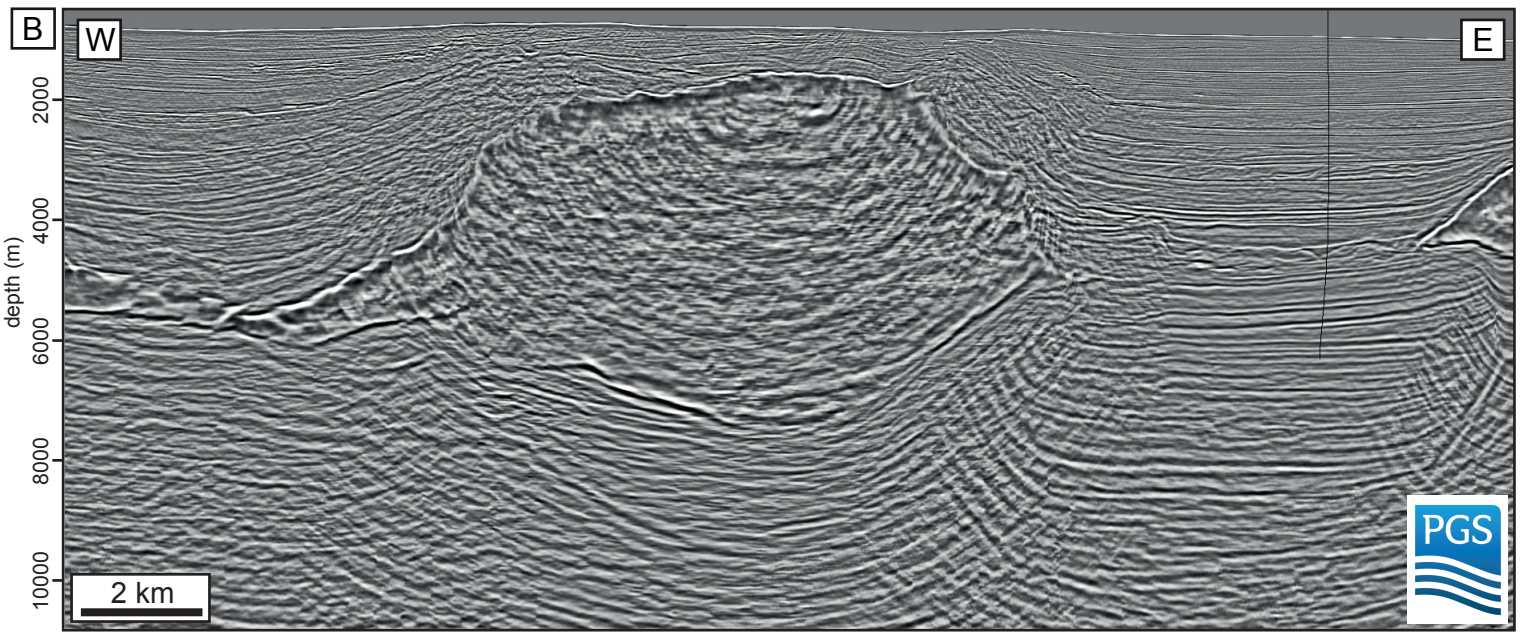
B
W
E
depth (m)
2000
4000
6000
8000
10000
2 km
PGS

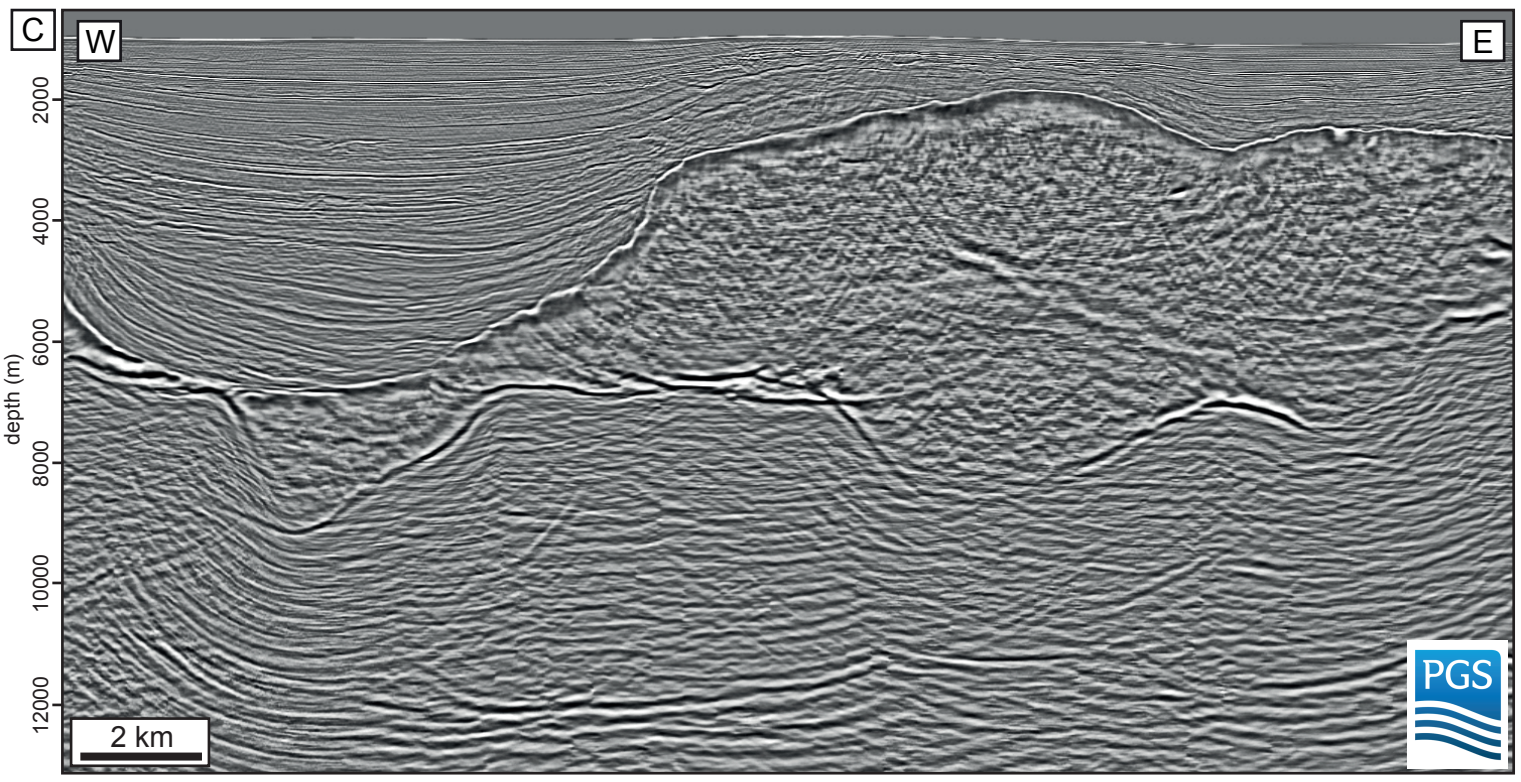
C
W
E
depth (m)
2000
4000
6000
8000
10000
12000
2 km
PGS

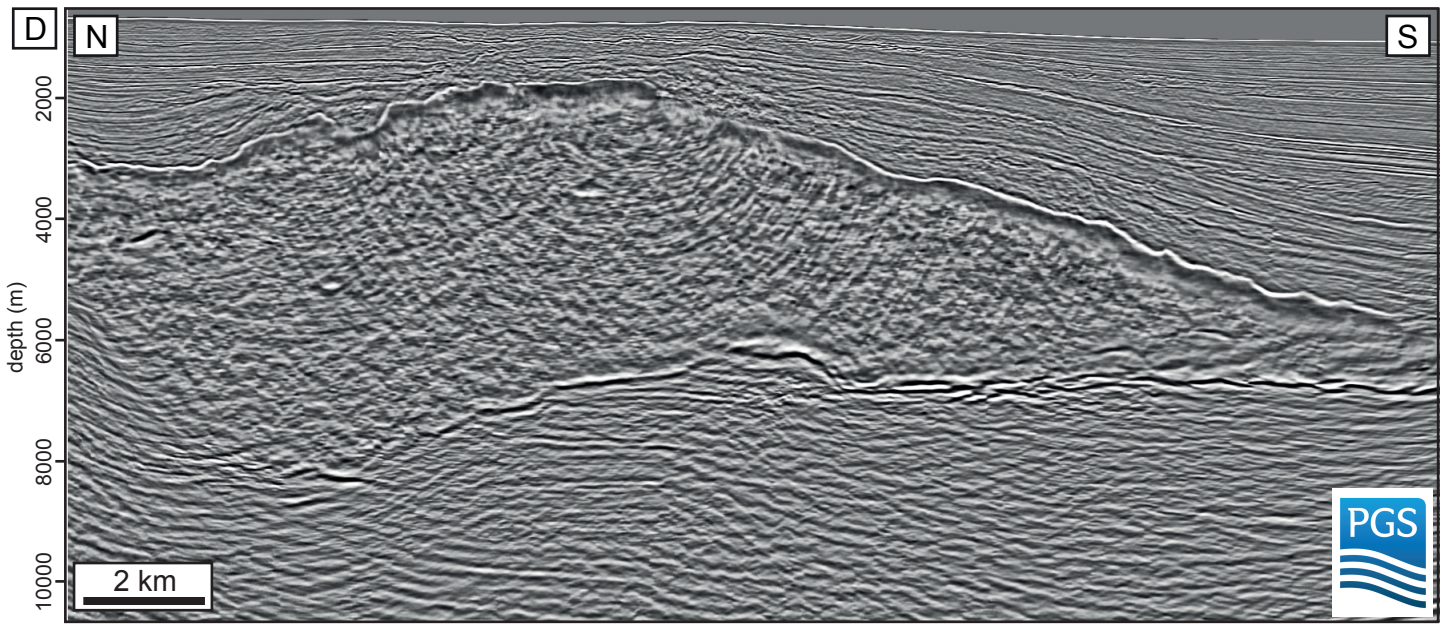
D
N
S
depth (m)
2000
4000
6000
8000
10000
2 km
PGS

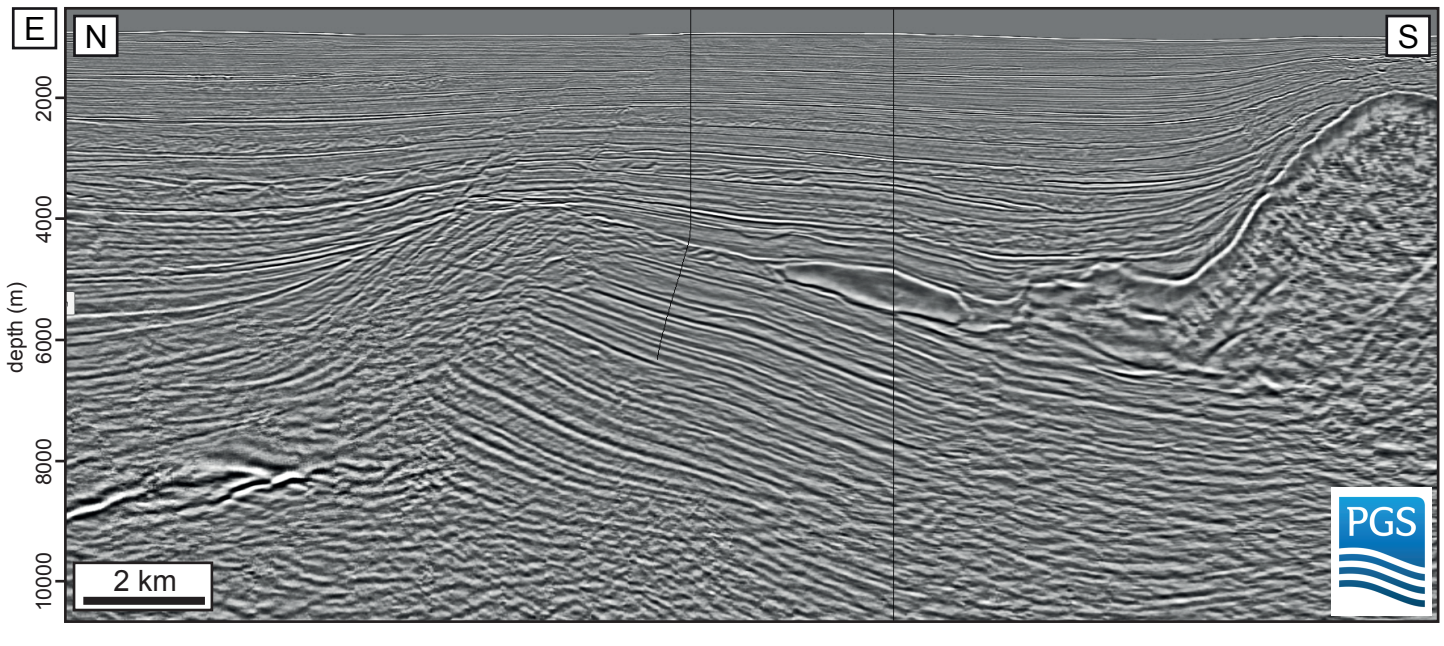
E
N
S
depth (m)
2000
4000
6000
8000
10000
2 km
PGS

Supplementary Material 2

	Depth			Biostratigraphic markers		Age		Notes
Report	MD (ft)	MD (m)	Pick Confidence	Foraminefera	Nannoplankton	Series	Stage	
1	5,221	1,591	POS	Globorotalia flexuosa		Upper Pleistocene	Ionian	
	8,159	2,487	DEF		Pseudoemiliania lacunosa "C" (acme)	Lower Pleistocene	Calabrian	
	8,160	2,487	DEF		Gephyrocapsa aperta (acme)	Lower Pleistocene	Calabrian	
	12,299	3,749	DEF		Helicosphaera sellii	Lower Pleistocene	Calabrian	
	12,300	3,749	DEF		Calcidiscus macintyrei	Lower Pleistocene	Calabrian	
	14,309	4,361	POS					unconformity
	14,310	4,362	DEF	Globoquadrina altispira		Upper Pliocene	Piacenzian	
	14,370	4,380	DEF		Sphenolithus abies	Lower Pliocene	Zanclian	
	14,430	4,398	DEF		Reticulofenestra pseudoumbilica	Lower Pliocene	Zanclian	
	19,620	5,980	DEF		Dictyococcites antarcticus	Lower Pliocene	Zanclian	
	20,159	6,144	POS					reworked material
	20,160	6,145	POS		Amaurolithus tricorniculatus	Lower Pliocene	Zanclian	
	20,959	6,388	POS					reworked material
2	5,280	1,609	DEF	Globorotalia flexuosa		Upper Pleistocene	Ionian	
	5,700	1,737	DEF					local marker foram increase
	6,060	1,847	DEF					local marker foram increase
	6,210	1,893	DEF					local marker foram increase
	6,390	1,948	DEF					local marker foram increase
	6,990	2,131	DEF					local marker foram increase
	7,740	2,359	DEF					local marker foram increase
	7,800	2,377	DEF					transported outer shelf facies
	8,160	2,487	DEF	Stilostomella antillea		Lower Pleistocene	Calabrian	
	9,660	2,944	DEF					local marker foram increase
	10,050	3,063	DEF					local marker foram increase
	10,110	3,082	DEF	Sphaeroidinella dehiscens (acme "A")		Lower Pleistocene	Calabrian	
	10,950	3,338	DEF					local marker foram increase
	12,510	3,813	DEF	Sphaeroidinella dehiscens (acme "B")		Lower Pleistocene	Calabrian	
	12,750	3,886	DEF	Uvigerina hispida		Lower Pleistocene	Calabrian	
	12,840	3,914	DEF					reworked material
	14,310	4,362	DEF	Globorotalia menardii (coiling change left/right)		Upper Pliocene	Gelasian	
	14,850	4,526	POS	Globorotalia miocenica		Upper Pliocene	Gelasian	
	15,090	4,599	POS	Globorotalia miocenica		Upper Pliocene	Gelasian	
	15,150	4,618	DEF	Globorotalia pertenuis		Upper Pliocene	Gelasian	
	16,140	4,919	POS			Upper Pliocene	Piacenzian	
	17,010	5,185	DEF	Cibicides grosseperforatus		Upper Pliocene	Piacenzian	
	17,550	5,349	DEF					local marker foram increase
	17,700	5,395	DEF	Cyclammina sp.		Upper Pliocene	Piacenzian	
	17,730	5,404	DEF	Arenaceous fauna		Upper Pliocene	Piacenzian	
	17,820	5,432	DEF	Cibicides marsi		Lower Pliocene	Zanclian	
	17,850	5,441	DEF	Globorotalia margaritae		Lower Pliocene	Zanclian	
	18,060	5,505	DEF	Uvigerina rustica		Lower Pliocene	Zanclian	
	18,119	5,523	DEF					reworked material
	18,120	5,523	DEF	Globigerina nepenthes		Lower Pliocene	Zanclian	
	18,330	5,587	DEF					local marker foram increase
	18,510	5,642	DEF					transported outer shelf facies
	18,660	5,688	DEF	Sigmoilina "P" / cf. schlumbergeri		Lower Pliocene	Zanclian	
	19,050	5,806	DEF					local marker foram increase
	19,590	5,971	DEF					local marker foram increase
	19,890	6,062	DEF	Sphaeroidinellopsis multiloba		Lower Pliocene	Zanclian	
	20,040	6,108	POS	Globorotalia menardii (coiling change right/left)		Upper Miocene	Messinian	
	20,190	6,154	DEF					
	20,430	6,227	POS	Globorotalia margaritae primitiva		Upper Miocene	Messinian	
3	9,660	2,944	DEF		Gephyrocapsa aperta	Upper Pleistocene	Ionian	
	10,860	3,310	DEF		Scyphosphaera pulcherima	Lower Pleistocene	Calabrian	
	11,550	3,520	DEF		Calcidiscus macintyrei	Lower Pleistocene	Calabrian	
	12,300	3,749	DEF		Helicosphaera sellii	Lower Pleistocene	Calabrian	
	13,890	4,234	DEF		Discoaster brouweri	Upper Pliocene	Gelasian	

DEF=definite
POS=possible

United States Department of Interior
Bureau of Ocean Energy Management
Biostratigraphic Chart of the Gulf of Mexico Offshore Region, Jurassic to Quaternary

BOEM Bureau of Ocean Energy Management

Recent through Oligocene

Time (mya) (not to scale)	System	Subsystem	Series	Stage	Foraminiferal planktic & benthic regional and local markers	Calcareous nannoplanktic regional and local markers	BOEM CHRONOZONE
	Quaternary		Holocene		Globorotalia inflata		
			Pleistocene	Ionian Upper	Globorotalia flexuosa Sangamon fauna	Emiliania huxleyi (base of acme) Pontosphaera indooceanica Gephyrocapsa oceanica flood Gephyrocapsa caribbeanica flood	PLU
0.20				Ionian Middle	Globorotalia truncatulinoides coiling change, right-to-left Trimosina "A"	Helicosphaera inversa Pseudoemiliania lacunosa "A" Pseudoemiliania lacunosa "B" Gephyrocapsa caribbeanica increase Gephyrocapsa omega Gephyrocapsa parallela Pseudoemiliania ovata	PLM
0.78				Ionian Lower / Calabrian	Stilostomella antillea Globorotalia incisa Sphaeroidinella dehiscens acme "A" Trimosina "A" acme Angulogerina magna Hyalinea balthica / Trimosina "B" Globorotalia tosaensis tosaensis Sphaeroidinella dehiscens acme "B" Angulogerina "B" Uvigerina hispida	Pseudoemiliania lacunosa "C" acme Gephyrocapsa aperta acme Scyphosphaera pulcherima, Gephyrocapsa caribbeanica (large) Helicosphaera sellii Lithostromation perdurum Calcidiscus macintyrei	PLL
1.77		Neogene	Pliocene	Upper / Gelasian	Globorotalia crassula acme, Globorotalia praehirsuta Cristellaria "S" Globorotalia menardii coiling change, left-to-right Globorotalia exilis Globorotalia miocenica Globorotalia pertenuis Bolivina imporcata / "P" Lenticulina 1 Textularia crassisepta / "P"	Discoaster brouweri, Calcidiscus macintyrei increase Discoaster brouweri "A" Discoaster pentaradiatus Discoaster surculus	PU
2.60				Upper / Piacenzian	Ceratobulimina pacifica Cassidulina laevigata carinata acme / "L" Haplophragmoides emaciatum Saracenaria "H" Globorotalia multicamerata Globoquadrina altispira = Valvulineria "H" Cyclammina sp. Arenaceous fauna Cibicides grosseperforatus Sphaeroidinellopsis seminulina Textularia 1	Discoaster asymmetricus Cycloperfolithus carlae, Discoaster tamalis	
3.58				Lower / Zanclian	Buccella (Eponides) hannai acme Cibicides marsi Globorotalia margaritae Uvigerina rustica Globigerina druryi / nepenthes "B" Globigerina nepenthes Bulimnella 1 Siphotextularia jugosa / "J" Sigmoilina "P" / cf. schlumbergeri Sphaeroidinellopsis multilobata Globigerinoides mitra Globorotalia plesiotumida acme	Sphenolithus abies Reticulofenestra pseudoumbilica, Discoaster intercalcaris, Dictyococcites antarcticus Pseudosphenolithus abies "B" acme Sphenolithus abies "B" Amaurolithus tricorniculatus Ceratolithus acutus Discoaster quintatus	PL
5.32				Messinian	Globorotalia menardii coiling change, right-to-left Globorotalia margaritae primitiva Globorotalia juanai Textularia "X" Textularia tatumi Bolivina denticulata	Discoaster quinqueramus Discoaster berggrenii Reticulofenestra rotaria Discoaster berggrenii "A"	
7.12			Miocene	Upper / Tortonian	Textularia 6 Bigenerina irregularis / 6 Globorotalia acostaensis coiling change, right-to-left Planulina renzi Reophax davepopei, Robulus "E" Bigenerina floridana / "A" Cristellaria "K" Melonis pompilioides increase Cibicides trincherasensis Uvigerina carapitana Amphistegina "E" Cyclammina 3 Globorotalia lenguaensis, Bolivina thalmanni Discorbis 12 Bigenerina "B" Eponides mansfieldi Textularia "G" Globoquadrina dehiscens Robulus 15 Textularia "L" Cibicides inflata Cibicides carstensi, Bigenerina 2 Globorotalia mayeri Globorotalia siakensis Uvigerina 3, Cibicides carstensi increase	Discoaster neohamatus Discoaster loeblichii Minylithus convallis Catinaster mexicanus Discoaster bellus, Discoaster calcaris Discoaster prepentaradiatus Discoaster prepentaradiatus increase Discoaster bollii, Catinaster calyculus Discoaster hamatus Catinaster coalitus Discoaster exilis Helicosphaera walbersdorfensis Coccolithus miopelagicus	MUU MLU
11.20				Middle / Serravallian	Globorotalia fohsi robusta Robulus 5 / 55 Textularia "W" Globorotalia fohsi lobata Globorotalia fohsi praefohsi Globorotalia fohsi fohsi Globorotalia peripheroacuta Bigenerina humblei Gyroidina miocenica Globorotalia peripheroronda Cristellaria "I" Praeorbulina glomerosa Cibicides opima	Discoaster kugleri Discoaster kugleri acme Calcidiscus premacintyrei Cyclicargolithus floridanus Discoaster sanmiguelensis Sphenolithus heteromorphus Discoaster petaliformis Sphenolithus heteromorphus acme	MUM MMM
14.80				Middle / Langhian	Robulus 53 Amphistegina "B" Globorotalia siakensis coiling change, left-to-right Globigerinatella insueta Robulus "L" / 43 Cibicides 38	Helicosphaera ampliaperta Discoaster deflandrei acme Discoaster calculosus	MLM
16.40				Lower / Burdigalian	Camerina 1, Robulus 54B = Cristellaria 54 Saracenaria sp. / "D" Gyroidina "K" / 9 / 4 Catapsydrax stainforthi Catapsydrax dissimilis, Robulus chambersi, Discorbis bolivarensis / "B", Cristellaria "A" Marginulina ascensionensis / "A" Globigerina binaensis Gyroidina 8 Siphogenerina fredsmithi	Sphenolithus belemnos Reticulofenestra gartneri Sphenolithus disbelemnos Orthorhabdus serratus Triquetrorhabdulus carinatus, Triquetrorhabdulus challengeri Discoaster calculosus increase	MUL MML
20.52				Lower / Aquitanian	Siphonina davisi Planulina palmerae Globigerinoides primordius Lenticulina hanseni Lenticulina jeffersonensis, Cristellaria "R", Globorotalia kugleri, Globigerina angulisuturalis	Discoaster saundersi Sphenolithus dissimilis Cyclicargolithus abisectus Helicosphaera recta	MLL
23.80	Paleogene		Oligocene	Upper / Chattian	Robulus "A" Discorbis gravelli Globigerina ciperoensis ciperoensis Heterostegina texana Cibicides jeffersonensis Bolivina perca Marginulina idiomorpha Marginulina vaginata Marginulina howei Camerina "A" Miogypsinoides "A" Cibicides hazzardi Globorotalia opima nana Globorotalia opima opima Cristellaria "H" Marginulina texana Bolivina mexicana	Dictyococcites bisectus Sphenolithus delphix, Ericsonia fenestrata Zyghrablithus bijugatus Sphenolithus ciperoensis Sphenolithus distentus	OU
28.50				Lower / Rupelian	Nonion struma Nodosaria blanpiedi Discorbis "D" Chiloguembelina cubensis Textularia mississippiensis seligi Anomalina bilateralis Globigerina ampliapertura Spiroplectammina mississippiensis Globorotalia increbescens Textularia warreni Pseudohastigerina micra Loxostoma "B" Cibicides pippeni Cibicides mississippiensis	Sphenolithus predistentus Helicosphaera compacta Sphenolithus pseudoradians, Reticulofenestra hampdenensis Reticulofenestra umbilica Reticulofenestra hillae Ericsonia formosa Ericsonia subdisticha Discoaster nodifer Ismolithus recurvus	OL
33.70							

Eocene through Jurassic

Time (mya) (not to scale)	System	Subsystem	Series	Stage	Planktic & benthic foraminifera & ostracod (O) regional and local markers	Calcareous nannoplanktic regional and local markers	BOEM CHRONOZONE
33.70	Tertiary	Paleogene	Eocene Upper	Priabonian	Globorotalia cerroazulensis cocoaensis, Hantkenina alabamensis Textularia hockleyensis Globorotalia cerroazulensis pomeroli Textularia dibollensis Globigerinatheka tropicalis / mexicana Globigerinatheka semiinvoluta Camerina moodybranchensis, Camerina jacksonensis	Discoaster saipanensis, Micrantholithus altus Discoaster barbadiensis Chiasmolithus consuetus Cribrocentrum reticulatum Sphenolithus obtusus	EU
37.00			Eocene Middle	Bartonian	Nonionella cockfieldensis Truncorotaloides rohri Discorbis yeguaensis Eponides yeguaensis Nodosaria mexicana Ceratobulimina eximia Morozovella lehneri Eponides guayabalensis Globorotalia bullbrooki Truncorotaloides topilensis Clavulinoides guayabalensis Operculinoides sabinensis Orbulinoides beckmanni Subbotina frontosa Acarinina broedermanni	Micrantholithus procerus, Chiasmolithus grandis, Pemma papillatum Pemma basquensis Pemma stradneri Pemma balium Sphenolithus radians Chiasmolithus solitus Chiasmolithus gigas	EM
41.30				Lutetian	Cyclammina cancriverensis Discocyclina advena Morozovella aragonensis Haplocytheridea stenzeli (O)	Discoaster sublodoensis, Sphenolithus spiniger Rhabdosphaera inflata Discoaster lodoensis	
49.00				Ypresian	Acarinina soldadoensis Morozovella quetra Acarinina angulosa Morozovella rex / subbotinae Morozovella formosa formosa Globorotalia wilcoxensis Morozovella acuta	Chiasmolithus californicus Tribrachiatus orthostylus Toweius crassus Tribrachiatus contortus Discoaster multiradiatus	EL
54.50			Paleocene Upper	Thanetian	Morozovella velascoensis Cytheridea sabinensis (O) Discorbis washburni Planulorotalites pseudomenardii Morozovella angulata Planulorotalites pusilla pusilla Planulorotalites compressa Vaginulina longiforma, Subbotina pseudobulloides Morozovella uncinata	Fasciculithus tympaniformis Heliolithus kleinpellii Heliolithus reidelii Toweius eminens Chiasmolithus bidens Discoaster diastypus	LU
57.90				Selandian	Vaginulina midwayana, Globorotalia inconstans		
60.90			Lower	Danian	Globorotalia trinidadensis Globoconusa daubjergensis Robulus pseudocostata Globigerina eugubina	Cruciplacolithus edwardsii Markalius inversus astroporus	LL
65.00	Cretaceous	Upper	Gulfian	Maastrichtian	Abathomphalus mayaroensis Globotruncana contusa Gansserina gansseri Rosita fornicata Globotruncana ventricosa Globotruncana lapparenti	Micula decussata Micula prinsii FAD Micula murus FAD Watznaueria barnesae FAD Nephrolithus frequens FAD Reinhardtes levis Tetralithus trifidus Tranolithus phacelosus Aspidolithus parcus constrictus	KUU
71.30				Campanian	Globotruncana calcarata Globorotalites micheliniana Globotruncana elevata Archaeoglobigerina bosquensis Stensioina exsculpta exsculpta Marginotruncana marginata Marginotruncana coronata Whiteinella baltica Planoglobulina taylorana	Reinhardites anthophorus "A" Eiffellithus eximius Aspidolithus parcus parcus Reinhardites anthophorus "B" Lithastrinus grillii Bukryaster hayi Broinsonia enormis Marthasterites furcatus	
83.50				Santonian	Dicarinella asymetrica Whiteinella inornata Marginotruncana sinuosa Hedbergella delrioensis Stensioina granulata granulata Dicarinella concavata, Marginotruncana renzi	Eprolithus floralis Zeugrhabdotus noeliae Lithastrinus moratus	
85.80				Coniacian	Dicarinella imbricata Whiteinella paradubia Hedbergella amabilis	Quadrum gartneri Stoverius achylosus	
89.00				Turonian	Dicarinella hagni Planulina eaglefordensis Helvetoglobotruncana helvetica Praeglobotruncana stephani, Helvetoglobotruncana praehelvetica	Chiastozygus platyrhethum Parhabdolithus achlyostaurion Calculites axosuturalis Parhabdolithus asper	KLU
93.50				Cenomanian	Globigerinelloides bentonensis Rotalipora cushmani Rotalipora greenhornensis Rotalipora appenninica Rotalipora reicheli Lenticulina gaultina, Fossocytheridea lenoirensis (O), Favusella washitensis Textularia rioensis Rotalipora gandolfii	Microstaurus chiastius Axopodorhabdus albianus Lithraphidites acutus Lithraphidites pseudoquatratus Coriollithon kennedyi	
98.90		Lower	Comanchean	Albian	Planomalina buxtorfi Rotalipora ticinensis Ticinella roberti Cythereis fredericksburgensis (O), Cyth. brevis (O) Cytheridea goodlandensis (O), C. oliverensis (O) Biticinella breggiensis Ammobaculites goodlandensis Dictyoconus walnutensis Eocytheropteron trinitiensis (O) Orbitolina texana Rehacythereis ? aff. R. glabrella (O)	Hayesites albiensis Braarudosphaera africana Braarudosphaera hockwoldensis Prediscosphaera columnata Crucicribrum anglicum Rucinolithus irregularis	KUL KML
112.20				Aptian	Ticinella bejaouaensis Planomalina cheniourensis Epistomina sp. Globigerinelloides algerianus Globigerinelloides blowi Schackoina cabri Globuligerina hoteriva Hedbergella sigali Choffatella decipiens	Eprolithus antiquus Conusphaera mexicana, Micrantholithus obtusus Nannoconus kamptneri Micrantholithus hoschulzii Nannoconus steinmanni Conusphaera rothii	KLL
121.00			Coahuilan	Barremian	Schuleridea lacustris (O) Clavihedbergella eocretacea	Nannoconus colomii Nannoconus abundans Calcicalathina oblongata Lithraphidites bollii	
127.00				Hauter.		Speetonia colligata Crucellipsis cuvilleri	
132.00				Valang.	Everticyclammina virginulina Schuleridea acuminata (O)	Tubodiscus verenae Rucinolithus wisei Diadorhombus rectus Micrantholithus speetonensis	
137.00				Berriasian	Hutsonia vulgaris / callahani (O) Pentaschuleridea pentagonalis (O)	Polycostella senaria Polycostella beckmanni	
144.20	Jurassic	Upper		Tithonian	Gallaecytheridea postrotunda (O) Bucicrenata italica increase Eoguttulina amygdalina, Epistomina uhligi Epistomina stellacostata	Hexalithus noelae	JU
150.70				Kimmer.	Epistomina mosquensis Alveosepta jaccardi	Stephanolithion bigotii bigotii Stephanolithion bigotii maximum	
154.10				Oxfordian	Globuligerina oxfordiana Lenticulina quenstedti Paalzowella feifeli	Discorhabdus jungii Stephanolithion speciosum	
159.40		Middle		Callovian	Reinholdella crebra Epistomina regularis Epistomina coronata	Stephanolithion hexum Watznaueria crucicentralis	JM
164.40							

BOEM Gulf of Mexico Resource Evaluation
Robert B. Witrock (504) 736-2718 or 1-800-200-GULF

For public release May 1, 2003

References used for Mesozoic and Cenozoic age determination and stratigraphic units

Armentrout, J. M., 1996, High resolution sequence biostratigraphy: examples from the Gulf of Mexico Plio-Pleistocene, in J. A. Howell and J. F. Aitken, eds., High-resolution sequence stratigraphy: innovations and applications: Geological Society Special Publication 104, p. 65-86.

Ascoli, P., 1984, Epistominid biostratigraphy across the Jurassic-Cretaceous boundary on the northwestern Atlantic shelf: Benthos 83, International Symposium on Benthic Foraminifera, Pau, p. 27-34.

Ascoli, P., C. W. Poag, and J. Remane, 1984, Microfossil zonation across the Jurassic-Cretaceous boundary on the Atlantic margin of North America, in G. E. Westermann, ed., Jurassic-Cretaceous biochronology and paleogeography of North America: Geological Association of Canada Special Paper 27, p. 31-48.

Bergen, J. A., and P. J. Sikora, 1999, Microfossil diachronism in southern Norwegian North Sea chalks: Valhall and Hod fields, in R. W. Jones and M. D. Simmons, eds., Biostratigraphy in production and development geology: Geological Society Special Publication 152, p. 85-111.

Berggren, W. A., D. V. Kent, C. C. Swisher III, and M.-P. Aubry, 1995, A revised Cenozoic geochronology and chronostratigraphy, in W. A. Berggren, D. V. Kent, M.-P. Aubry, and J. Hardenbol, eds., Geochronology, time scales and global stratigraphic correlation: Society of Economic Paleontologists and Mineralogists Special Publication 54, p. 129-212.

Bolli, H. M., J. B. Saunders, and K. Perch-Nielsen, eds., 1985, Plankton stratigraphy, volume 1: planktic foraminifera, calcareous nannofossils and calpionellids: Cambridge, Cambridge University Press, 509 p.

Bolli, H. M., J.-P. Beckmann, and J. B. Saunders, 1994, Benthic foraminiferal biostratigraphy of the south Caribbean region: Cambridge, Cambridge University Press, 408 p.

Bralower, T. J., R. M. Leckie, W. V. Sliter, and H. R. Thierstein, 1995, An integrated Cretaceous microfossil biostratigraphy, in W. A. Berggren, D. V. Kent, M.-P. Aubry, and J. Hardenbol, eds., Geochronology, time scales and global stratigraphic correlation: Society of Economic Paleontologists and Mineralogists Special Publication 54, p. 65-79.

Breard, S. Q., M. Nault, and A. D. Callender, 1994, Biostratigraphy and paleoecologic tolerances of Oligocene Paleocene foraminiferal assemblages of the Gulf Coast basin: Gulf Coast Association of Geological Societies Transactions, v. 44, p. 111-116.

Breard, S. Q., A. D. Callender, and M. Nault, 1997, Application of bathyal foraminiferal events to the Neogene through Pleistocene biostratigraphic framework of the Gulf of Mexico basin: Gulf Coast Association of Geological Societies Transactions, v. 47, p. 66-73.

Breard, S. Q., A. D. Callender, and M. Nault, 2000, Gulf of Mexico basin Late Tertiary deep-water biostratigraphic zonation: relationship to standard shelf foraminiferal and calcareous nannofossil marker terminology: Gulf Coast Section Society of Economic Paleontologists and Mineralogists Foundation Twentieth Annual Research Conference Deep-water Reservoirs of the World, December 3-6, 2000, Houston.

Brenchley, P. J., and D. A. T. Harper, 1998, Palaeoecology: ecosystems, environments and evolution: London, Chapman and Hall, 402 p.

Catalano, R. E., E. Di Stefano, A. Sulli, F. P. Vitale, S. Infuso, and P. R. Vail, 1998, Sequences and system tracts calibrated by high-resolution bio-chronostratigraphy: the central Mediterranean Plio-Pleistocene record, in P.-C. de Graciansky, J. Hardenbol, T. Jacquin, and P. R. Vail, eds., Mesozoic and Cenozoic sequence stratigraphy of European basins: Society of Economic Paleontologists and Mineralogists Special Publication 60, p. 155-177.

Frizzell, D. L., 1954, Handbook of Cretaceous foraminifera of Texas: Bureau of Economic Geology Report of Investigations 22, 232 p.

Gradstein, F. M., 1976, Biostratigraphy and biogeography of Jurassic Grand Banks foraminifera: Maritime Sediments Special Publication, v. 1B, p. 557-583.

Gradstein, F. M., F. P. Agterberg, and M. A. D'Iorio, 1990, Time in quantitative stratigraphy, in T. A. Cross, ed., Quantitative dynamic stratigraphy, p. 519-542.

Gradstein, F. M., F. P. Agterberg, J. G. Ogg, J. Hardenbol, P. van Veen, J. Thierry, and Z. Huang, 1995, A Triassic, Jurassic and Cretaceous time scale, in W. A. Berggren, D. V. Kent, M.-P. Aubry, and J. Hardenbol, eds., Geochronology, time scales and global stratigraphic correlation: Society of Economic Paleontologists and Mineralogists Special Publication 54, p. 95-126.

Jones, R. W., 1996, Micropalaeontology in petroleum exploration: Oxford, Oxford University Press, 432 p.

Jones, R. W., and M. D. Simmons, eds., 1999, Biostratigraphy in production and development geology, Geological Society of London Special Publication 152, 318 p.

Lawless, P. N., R. H. Fillon, and R. G. Litton III, 1997, Gulf of Mexico Cenozoic biostratigraphic, lithostratigraphic, and sequence stratigraphic event chronology: Gulf Coast Association of Geological Societies Transactions, v. 47, p. 271-282.

Lord, A. R., ed., 1982, A stratigraphic index of calcareous nannofossils: Chichester, British Micropalaeontological Society, 192 p.

Picou, E. B., Jr., B. F. Perkins, N. C. Rosen, and M. J. Nault, eds., 1999, Gulf of Mexico basin biostratigraphic index microfossils - a geoscientist's guide: foraminifers and nannofossils, parts I and II, Oligocene through Pleistocene foraminifers: Gulf Coast Society of Economic Paleontologists and Mineralogists Foundation, 215 p., 3 charts, 2 tables of synonyms (Text and CD-ROM).

Prothero, D. R., 2001, Magnetostratigraphic tests of sequence stratigraphic correlations from the southern California Paleogene, Journal of Sedimentary Research, v. 71, p. 526-536.

Simmons, M. D., W. D. Berggren, R. O. Koshkarly, B. J. O'Neill, R. W. Scott, and W. Ziegler, 1997, Biostratigraphy and geochronology in the 21st century: Paleontology in the 21st century, an International Senckenberg Conference and Workshop, reports and recommendations. http://www.nhm.ac.uk/hosted_sites/paleonet/paleo21biostrat.html

Stainforth, R. M., J. L. Lamb, H. Luterbacher, J. H. Beard, and R. M. Jeffords, 1975, Cenozoic planktonic foraminiferal zonation and characteristics of index forms: University of Kansas Paleontological Institute, Article 62, 162 p.

Styzen, M. J., 1996, Late Cenozoic chronostratigraphy of the Gulf of Mexico: Gulf Coast Society of Economic Paleontologists and Mineralogists Foundation, chart, 2 sheets.

Total Biostratigraphic Services, 1994, Miocene/Oligocene biostratigraphic chart (Gulf of Mexico): Total Biostratigraphic Services, Inc., New Orleans.

Waterman, A. S., 1999, Biostratigraphic chart, Gulf of Mexico Neogene (version 9909): Paleo-Data, Inc., New Orleans.

Wood, L. J., 2000, Chronostratigraphy and tectonostratigraphy of the Columbus basin, eastern offshore Trinidad: American Association of Petroleum Geologists Bulletin, v. 84, p. 1905-1928.

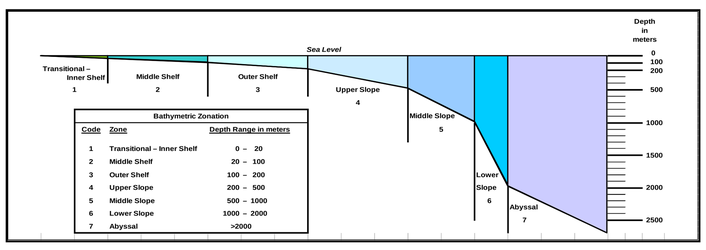

LEGEND

All foraminiferal markers are extinction points (LADs) unless otherwise indicated.
(O) indicates an ostracode species.
The calcareous nannoplanktic markers are mainly coccolith species LADs. Dinoflagellates and palynomorphs (pollen) are occasionally used.
LAD: **L**ast **A**ppearance **D**atum
FAD: **F**irst **A**ppearance **D**atum
Species LADs separated by a virgule (the diagonal mark "/") indicates either synonymous species or synchronous species.
Species LADs separated by "=" indicates synchronous species.
Two or more species LADs separated by a comma indicate synchronous species LADs.
(for example, Discoaster bollii, Catinaster calyculus are two separate but time-equivalent coccolith extinction points).
BOEM Chronozone: A body of rock formed during the same time span, bounded by biostratigraphic or correlative seismic markers.

References to this chart should be as follows:
Witrock, R. B., L. D. Nixon, P. J. Post, and K. M. Ross, 2003, Biostratigraphic Chart of the Gulf of Mexico Offshore Region, Jurassic to Quaternary, U. S. Department of the Interior, Bureau of Ocean Energy Management, New Orleans, Louisiana.

Supplementary Material 4